Precision Positioning in Unmanned Aerial Geophysics

Luke Thomas Smith, BSc

Department of Earth and Planetary Science

Macquarie University

9th of October 2017

Statement of Originality

This work has not previously been submitted for a degree or diploma in any university. To the best of my knowledge and belief, the thesis contains no material previously published or written by another person except where due reference is made in the thesis itself.

_____   _____

Contents

Abstract

This research investigates the implementation of precision GPS in Unmanned Aerial Vehicles (UAV) for use in geophysical exploration. The prompt for this research was the Desert Fireball Network's meteorite recovery program, where an advanced impact site prediction system is followed by manual search and recovery. A small, automated, search vehicle is needed to explore the likely impact zones, which would require precise and accurate positioning in conjunction to its sensor capabilities. This thesis presents a Kalman filter implementation to improve and interpolate positioning during post-processing. This thesis also presents a sub-2kg UAV magnetometer system utilising an RTK GPS to achieve centimetric positioning. An RTK GNSS module was integrated with an Arduino microcontroller for acquisition of in-house magnetometer gradiometer data. Results are presented for two field trials, testing both positioning and magnetometer performance. The magnetometer performance was limited, particularly due to flight effects and sensitivity, however under ideal conditions the system would be capable of locating a meteorite sample. Dropout of DGPS during flight did occur during surveys, but the Kalman filter was successful in ameliorating the effects.

Acknowledgements

I'd like to thank my Supervisor, Craig O'Neill for his enthusiasm and expertise throughout my Masters, as well as my undergraduate studies. I'd like to extend my appreciation to the other staff and students at Macquarie University for their knowledge and support, as well as their friendship. A big thankyou to my grandfather for sparking my love of Earth Sciences, my brother for inspiring me to get airborne, and my family, friends, and Jess for keeping me grounded.

Chapter 1 - Introduction

Airborne geophysics has been reimagined in recent years, with the advent of Remotely Piloted Aircraft (RPA), also known as UAVs or drones. The technology powering UAV's has progressed rapidly with their increasing adoption in industry and consumer applications, with applications across fields such as agriculture, media and geophysical exploration. The typical approach in geophysical exploration has been to build a large system to carry industry standard, bulky equipment with more restrictive drone operating licences and costs. Likewise, most precision positioning equipment is too heavy to be integrated with a small system and not optimised for rapidly moving aircraft.

This thesis presents research into the development of a very small RPA (<2 kg) system utilising a magnetometer gradiometer array and a centimetric GPS receiver, and comments on its application to meteorite detection. This was prompted by Macquarie University's recent association with the Australian Desert Fireball Network.

The Desert Fireball Network (DFN) is a meteorite tracking and retrieval network, with 51 stations spread across 3 million km² of central Australia. It is hoped an RPA magnetometer system will aid in rapidly locating these meteorites. Despite the fantastic tracking and impact prediction work done by the DFN (e.g., Howie et al., 2017), it is impossible to determine the exact landing site of a meteor due to motion during "dark flight", where the meteor is no longer visible after it has slowed through the atmosphere. Aerial spotting has been successfully utilised in the past via chartered tour planes, which come with considerable costs. The successful identification of an impact site (e.g., Figure 1) was made possible by obvious debris field around the small crater in the soft sediment of the landing site. In situations where the ground is hard or vegetated, little to no crater may be present, which presents much harder targets for a solely visual search. The magnetic approach bears no reliance on impact craters and can theoretically detect partially buried or covered meteorites. An airborne camera can augment the magnetic system, and live video systems are already commonly incorporated on RPAs.

Figure 1: Debris field around the Murrili meteorite as seen from a chartered plane. Feature approx. 40cm diameter. Image: Fireballs in the Sky, 2016. Fall and recovery described in Bland et. al., 2016.

Meteorites are good target for magnetic techniques, because fresh meteorites are located on or near the surface, and are anomalous to the surrounding surface material. Meteorites currently recovered by the Australian Desert Fireball Network include a 1.2 kg chondrite (*Dingle Dell*), a 25 g chondrite (*Mason Gully*), a 1.7 kg chondrite (*Murrili*) and 324 g of achondrite in two fragments (*Bunburra Rockhole*). Iron meteorites show a very large magnetic response (Macke, 2010) and are often visually distinctive, however chondrites (Susceptibilities between 2.4 to 5.7 logχ) (Smith et al., 2006) may still contrast magnetically with the surrounding lithologies. In order to capture the localised magnetic response of a small meteorite in a noisy environment, such as on a UAV, it is important to acquire precise magnetic response positions. The grouping of several high readings in a single precise location will cause the anomaly to persist through filtering and gridding. This is realised through the use of a miniature differential GPS module.

Micro-geophysics surveys require highly accurate and precise positioning, which can be achieved by satellite positioning. Common single sensor positioning provides several meters precision at best, but advanced techniques such as differential or dual frequency positioning can provide accuracy to centimetre scales. Differential techniques use two commercial grade receivers to account for signal path variances through the atmosphere, while dual frequency utilises multiple broadcast satellite signals. These technologies have been utilised for many years, however only recently have miniature systems, such as the Emlid Reach RTK GPS (Figure 2) become available.

The Emlid Reach module is a single frequency, carrier wave positioning device that can utilise a second module or other correction providers for differential operation. The receiver operates the open source *RTKLIB* program (Takasu and Yasuda, 2009) and is readily integrated with an Arduino micro-controller via serial output and 5V power requirement.
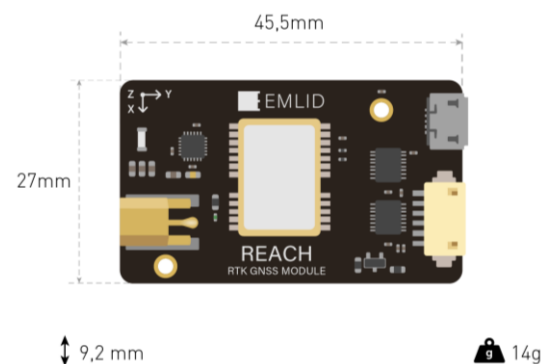
Figure 2 - Emlid Reach RTK GNSS Receiver. Emlid, 2017

Despite the improved resolution offered by differential GPS, some location data returned remains incongruous with the known ground track, as a result of normal receiver behaviour. That is, a typical GPS receiver is optimised for single point positioning, not for recording a dynamic ground track. For example, if a new satellite comes into view, the receiver may update its best estimated location which is manifested as an abrupt change in ground track (e.g., Figure 3). While the position may or may not be more accurate, the deviation from the line will affect the overall gridded response. In this thesis several common positioning errors in data acquired from a

commercial differential RTK GPS are observed and mitigated via the use of a Kalman filter. The effects on geophysical gridding by reducing these path errors is investigated by gridding data from a magnetometer gradiometer array, which obtains positioning information from the GPS module.

To reduce the position offsets in the recorded GPS track, a Kalman filter is applied. The Kalman filter (Kalman, 1960) is a Bayesian estimation algorithm that combines measurements and predictions to estimate the most likely state of a system at any time. A system may be any set of observable data that are understood well enough to design a mathematical model for them, such as a constant voltage with noise, the flight of an Apollo rocket, or a GPS receiver tracking several

Figure 3 - Satellite count during surveying. Deviations are present when a satellite is lost, and a new best fit location is determined.

satellites and returning a position. In this instance, the Kalman filter operates on the GPS output track, designed to reduce positioning errors arising from the use of a fast-moving UAV. A Kalman filter is also utilised for noise reduction on the in-house magnetometer gradiometer, developed as a product of this research. It is important to note that GPS receivers already incorporate a Kalman filter, which fuses satellite distance measurements and uncertainty information to calculate a best position solution. The Kalman filter presented here takes past position information and other location indicators to remove sharp deviations in a recorded GPS track. It is hoped a filtered track will enhance the quality of magnetic gridding outputs.

Magnetic gradiometry was targeted for this thesis as it is ideal for detecting surface anomalies, and has several advantages over other magnetic techniques. Namely, gradiometry rejects noise that is common across sensors, is less affected by orientation changes, is sensitive across the array area, and is less sensitive to deeper bodies (in the Bz axis). It has several drawbacks, including a reduced capacity to locate deep features and it cannot return values for total magnetic intensity. These however are not necessary for surface target detection. The sensors used for the array are uniaxial fluxgate magnetometers, which are lightweight and solid-state components that are easily integrated with an Arduino microcontroller.

The fluxgate magnetometer gradiometer was constructed on campus, utilising four Stefan Mayer FLC-100 magnetometer, with an advertised accuracy of ±2% ±300 nT. The system was controlled
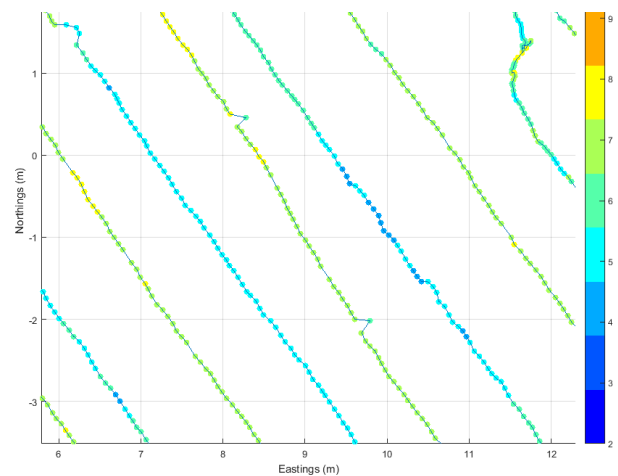
by an Arduino microcontroller, and incorporated the RTK GPS receiver for positioning. This sensor was used to collect all data presented in this thesis. Its low weight and minimal power consumption means it can be carried by a small (<2 kg) UAV, which allows unlicensed operation in Australia. The systems low weight will also increase flight times and handling, as a reduced cross section compared to standard equipment will minimise the impact of wind on the system.

1.1 Thesis Aims:

I. Develop software for magnetic and position data collection and analysis, including the Kalman filtering of GPS tracks

II. Construct a UAV platform incorporating differential GPS for magnetic gradiometry

III. Conduct trials of the system to demonstrate its application in locating meteorites

1.2 Thesis Structure:

This thesis encapsulates the combined goals of developing a functional geophysical sensor and the specific use of the Kalman filter in reducing positional noise from an RTK GPS receiver.

Chapter 2 presents the background on satellite navigation, precision techniques, and sources of error, and an overview of the general Kalman filter.

Chapter 3 presents the methodology, including an explanation of the GPS equipment used in testing and field operation, the Arduino microcontroller code, and the platform as a whole.

Chapter 4 presents results from a case study field survey, performed on physical meteorite samples. Data from this and other trial surveys will be presented.

Chapter 5 presents a discussion of Kalman filtering positional data and magnetic data, as well as the overall performance of the system.

Chapter 6 is an executive summary and conclusion, in which comment is made on the suitability of such a system to locating anomalous surface objects, such as meteorites.

Chapter 2 - Background

Many geophysical techniques have used satellite positioning for several decades. For example, a traditional surveyor's system comprises a bulky GPS unit atop a mast, held static for a period of time while an accurate position is recorded. The use of such a system is not available to an aerial platform due to the impact such a unit would have on flight dynamics, and as such a new approach was necessary. In this study, the use of a high-performance GPS with a Kalman filter was chosen to improve the positional accuracy of a dynamic system. An overview of such global navigation satellite systems, and the Kalman filter is presented here.

2.1 Global Navigation Satellite Systems

Global Navigation Satellite Systems (GNSS) are groups of satellites in semi-geosynchronous orbits that provide ranging information to devices on Earth. This ranging information can be used by receivers to determine positions accurate to several metres anywhere on Earth. The first global coverage system, or constellation, was the American "Global Positioning System" (GPS), from which the colloquial for satellite navigation systems "GPS" is derived. There are several other independently operated but simultaneously accessible systems, including Global Navigation Satellite System (GLONASS), Beidou and Galileo, as well as several augmentation systems (Groves, 2013). These programs are operated by nations and organisations other than the USA; Russia, China and the European Union respectively. GNSS' are passive, meaning there is no limit on the number of receiving devices, and no requirement for two-way communication from the user segment. Satellite navigation has become a routine feature of the modern world, used by billions every day for personal and commercial navigation and positioning. These same uses are exhibited in scientific applications across many disciplines. In Earth sciences, accurately recorded sample locations are necessary to recreate representative maps of the sampled feature.

2.1.1 GNSS Design

The basic principle of satellite navigation is the time of flight (TOF) measurement of radio signals broadcast by GNSS satellites. When the satellites orbital position is accurately known, distance to the satellite can be determined by the TOF multiplied with the speed of light (Groves, 2013). In GNSS, transmission time and satellite orbits are detailed in the transmitted radio message. To obtain a 3-dimensional location, or "fix", a minimum of four satellites in view are required, with the range to each constraining the possible location (Figure 4). In practice, more than 4 satellites

are utilised simultaneously and the best possible solution is determined. Radio signals broadcast by GNSS satellites have several components modulated onto a base carrier wave. The specific technology used by each GNSS implementation varies, but for a general background in satellite navigation the American Global Positioning System will be described here. For a detailed description of each system, see Groves (2013) or Hofmann-Wellenhof et al. (2007).
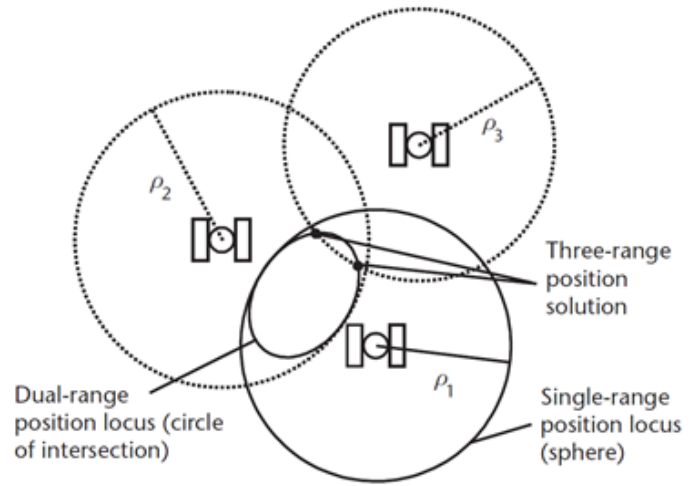

Figure 4 - Trilateration of position via Pseudorange (rho) measurements, Groves (2013)

There are several GPS radio signals broadcast on separate carrier wave frequencies, each modulated with several components. The first component is a pseudo-random noise (PRN) pattern common between satellites and receivers which is used to correlate the transmitted signal. The second component is the navigation data, which is encoded with the PRN as an exclusive-or function. This resulting wave form is then modulated onto the carrier wave to generate the transmission signal (Figure 5). As technology and usage requirements evolve, so do the carrier and codes broadcast by each generation of GNSS satellite. GPS carrier waves operate in the 1 to 2 GHz frequency range, referred to as the L (Link) Band, from which the following L1 through L5 bands are termed. Standard GPS receivers utilise navigation information coded onto the L1 carrier wave (1575.42 MHz), which forms the original and still predominantly used L1 C/A code (GPS Directorate, 2016). The C/A code contains two components, the ephemeris and almanac. The
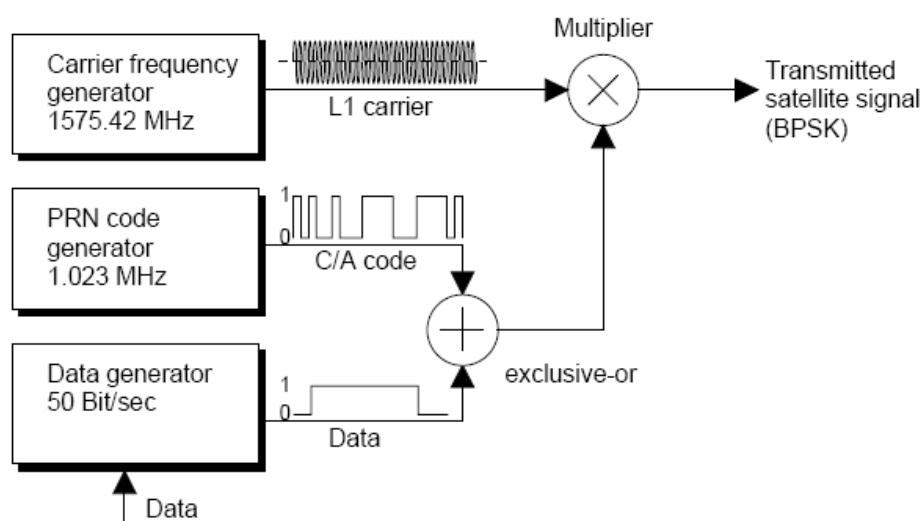

Figure 5 - Generation of the GPS Signal. BPSK indicates Binary Phase Shift Keying, a signal mode used in GNSS. From: National Instruments (2016)

transmitting satellite's precise orbital parameters and timing information are detailed in the ephemeris. Approximate details for other GPS satellites' status and orbits, as well as modelled ionospheric delay parameters are provided in the almanac. Using the L1 C/A signal alone gives an accuracy of approximately 15 m (Groves, 2013).

Several new carrier frequencies and codes are being provided by the GPS program as a continual modernisation in response to improvements in hardware and increasing demands of the increasing user population. The modernised bands are L2C, L5 and L1C, which are currently in "pre-operational" state. They will offer enhanced accuracy, higher power and error correction, and when used in conjunction offer sub meter accuracy from GPS alone (GPS.gov, 2017). GLONASS also undergoes continual upgrade, while Galileo and Beidou are in the final stages of constellation construction and will incorporate signals comparable to modernised GPS and GLONASS.

2.1.2 Satellite Augmentation:

There are a number of ground or satellite based augmentation systems (SBAS) in place for different regions to enhance positional accuracy and provide faster and more stable fixes. These include QZSS (Quasi-Zenith Satellite System - Japan through Australia) and WAAS (Wide Area Augmentation System – North America), which can be utilised to enhance other constellations on most modern receivers to return an accuracy of several metres in typical use. Other augmentation systems are used to ensure the operation of life critical applications, such as aircraft positioning and search and rescue. WAAS implements satellite broadcast differential correction from a ground station network to WAAS capable receivers, and is used to ensure aircraft navigation safety. QZSS is a system of three satellites in orbits designed to always retain one above 60 degrees elevation over Japan. Each QZSS satellite broadcasts standard ranging information on L1, L2 and L5, as well as accurate GPS constellation orbits. This arrangement assists with the use of receivers in Japan's "urban canyons", where the sky view is often obstructed by skyscrapers.

2.1.3 Sources and Mitigation of Location Error

There are many phenomena that reduce the accuracy of GNSS receivers, most of which are caused by the radio signal's path, and some of which are technological limitations. These location errors are exhibited as the difference between a unit's real position and its calculated position. The total location error is the sum of many small uncertainties from separate sources. Some of these can be accounted and corrected for, while others cannot be reduced with current satellite navigation technology (Ranacher et al. 2016).

2.1.3.1 Atmospheric error sources

At an orbital radius beyond 25,000km, GNSS signals must pass through the entirety of the Earth's atmosphere, including the charged-particle rich ionosphere. In the simplest case, the signal path from a satellite to a receiver is a straight line. This is not realised in practice, because refraction and reflection through the atmosphere lengthen the travel path and therefore travel time. This
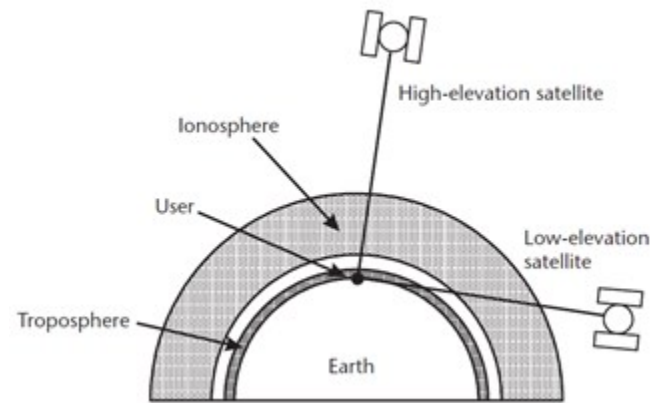

Figure 6 - Signal path through the atmosphere (Groves, 2013)

lengthening is proportional to the elevation of the satellite, due to the low elevation the signal must travel through more atmosphere (Figure 6), and hence is subject to greater path error.

Radio waves experience refraction throughout the atmosphere, and in the ionosphere they also display dispersive properties, in that their velocity is a function of their frequency. The difference in frequency between the carrier and the modulated wave causes divergence of the two, resulting in a satellite range error of 1-15 m depending on the time of day (Groves, 2013). However, utilising two different GNSS carrier frequencies can provide an accurate indication of the total delay caused by the ionosphere, because each carrier is dispersed according to its frequency. The total dispersion can be calculated to determine the ionospheric path length. Single frequency receivers rely on ionospheric model parameters broadcast as part of navigation messages to account for delays in the upper atmosphere, which can reduce atmospheric uncertainties by half (Groves, 2013).

2.1.3.2 Satellite specific uncertainties

Each GNSS satellite in a constellation is monitored and maintained constantly, with almanac information updated regularly. Regardless, small uncertainties are inherent to the satellite transmitted data. Timing and orbital data broadcast in the ephemeris are subject to the accuracy monitoring stations can provide, and the time it takes to update each satellites broadcast message. It is important to note the transmitted orbital parameters are estimated values, with satellite orbital positions accurate to approximately 100 cm (IGS, 2017a). GNSS monitoring stations are erected around the world to more tightly constrain these data. It is also possible to post-process satellite observations with more accurate satellite orbital data, calculated from measurements after the time of GPS observation (Dow et al., 2009).

On board satellites, atomic clocks maintain very accurate time measurements. However any delay between satellite, receiver and UTC base time directly transforms into a range error. Each new generation of satellite uses more accurate atomic clocks in an effort to minimise this error.

2.1.3.3 Multipath and Radio Interference Errors

GNSS navigation relies on line of sight (in the L band) to the transmitting satellite in order to receive accurately ranged signals. Many surfaces reflect or absorb L band frequencies, and as such a receiver may receive signals that have been reflected from the ground, buildings or equipment and personnel nearby. These objects may also block signals entirely. By design, GNSS signals are right hand circularly polarised (GPS Directorate, 2016), the purpose of which is to allow a well-designed antenna to reject left hand polarised signals - such as those generated by reflections of the original signal (Groves, 2013). The easiest way to reduce multipath error is to operate in an environment free from reflective features, and to provide a sufficient ground plane to block local ground reflections. Beyond this, longer observation times are necessary to average out errors arising from multipath errors.

Radio interference can diminish the ability for a receiver to acquire a fix, because noise reduces the certainty in correlation between the received satellite signal and receiver generated signal. Antennas and systems are therefore designed to diminish the susceptibility to noise (Groves, 2013). In addition, government authorities around the world, e.g., the Australian Communications and Media Authority, are responsible for allocating portions of the radio frequency spectrum for different applications. This works to prohibit other radio devices from emitting at frequencies reserved for use as GNSS signals.

2.1.3.4 Satellite geometry

The arrangement of satellites in view is an important consideration, and is indicated by a geometric factor termed the *Dilution of Precision – DOP* (Groves, 2013). Satellites distributed across a range of elevations and azimuths will more tightly constrain a position solution than one where satellites are clustered within one region of the sky view (e.g., Figure 7). Satellite arrangement and count are the only factors in minimising Dilution of Precision.

2.1.4 Error reduction techniques

In addition to individual error mitigation techniques as described above, several methods have been developed that utilise existing signals to achieve sub-metre accuracy, such as the use of differential receivers, or a combination of broadcast frequencies.
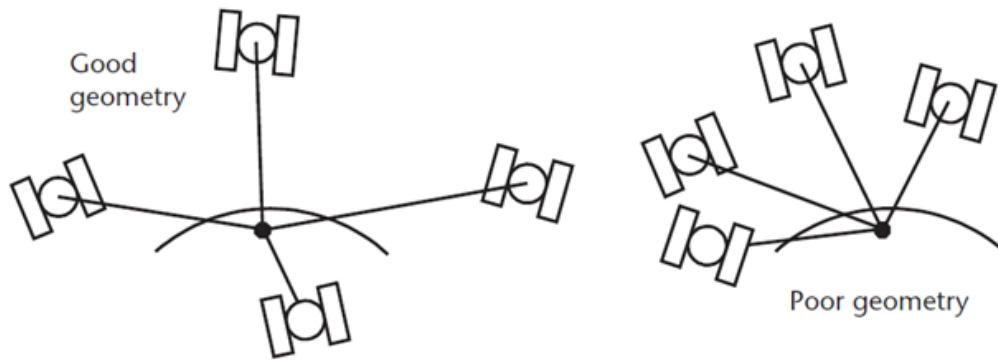
Figure 7 - Satellite Geometry determines the dilution of precision (DOP). A wide distribution of satellites across the sky view returns a small dilution of precision, while clustered satellites return a high DOP. (Groves, 2013)

2.1.4.1 Differential GNSS

A differential or DGPS system utilises two receivers, one at a known location, referred to as the base station, and a moving unit, known as the rover. Both receivers can have similar satellites in view across distances beyond a hundred kilometres, due to the high orbits of GNSS satellites. When a receiver is located at an accurately known and predetermined location, the offset from its satellite derived location can be assumed to be similar to all receivers within several kilometres (Groves 2013). The offset between the known and calculated position is then broadcast to GPS receivers within the area, whose locations are then corrected to a more accurate position (Figure 8). This method minimises the error from local atmospheric effects for all satellite signals common between the base and rover, and the second receiver present in the base allows carrier phase integer ambiguity resolution, as described below. Throughout this text, DGPS may be referred to as a "Fix" or "Float". Both terms refer to differential GNSS operation, however in Float status integer ambiguity is not resolved (Groves, 2013). In the Reach software, Fix further refers to the differential solution being over 3 times more likely than the next best fit solution (Emlid, 2017).
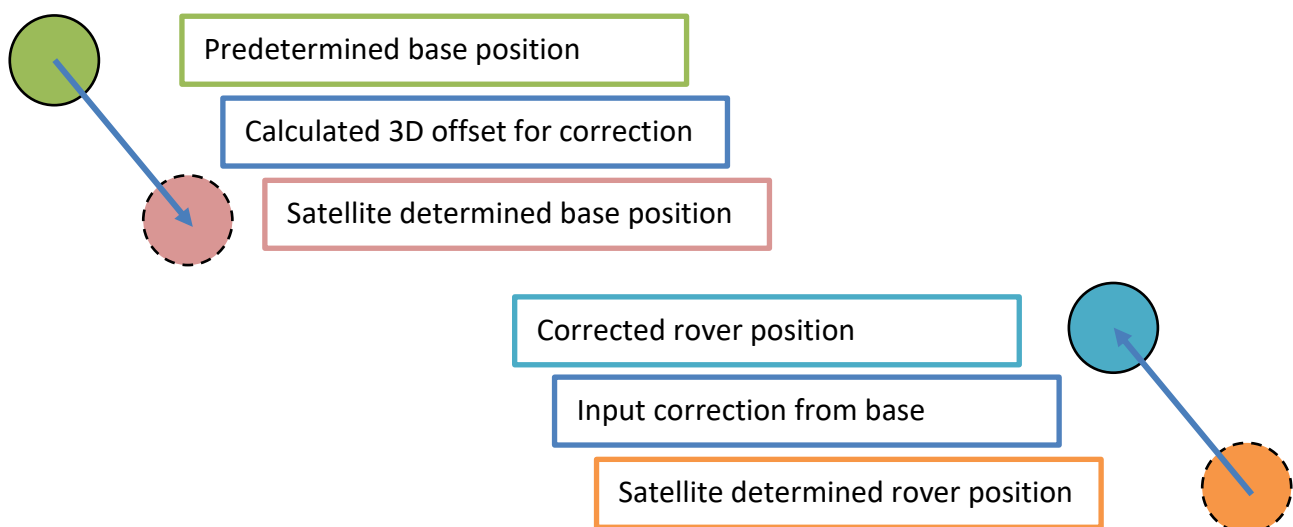

Figure 8 - Differential correction of receiver position. Determination of base station can be performed by long term satellite position averaging, using differential GPS from another known location, or alternative navigation techniques. The accuracy of the base limits the maximum accuracy of any rovers that use it.

DGPS performance degrades with increased base-receiver separation, or "baseline", at an approximate rate of +1 mm error per km (Takasu and Yasuda, 2009). This results in sub-decimetre relative accuracy up to 100 km. However, when using RTK a maximum baseline of 20 km is still recommended (ICSM, 2016). It is important to note the rover's accuracy is intrinsically tied to the accuracy of the base station, as it serves as the reference point for corrections.

It is possible for a GNSS base station to transmit corrections to any number of devices simultaneously. Permanent stations for this purpose are termed *CORS* – Continually Operating Reference Stations (Yan et al., 2009). These stations are often commercially operated, or made available by government agencies. They utilise calibrated receivers in accurately and precisely known locations, and may be accompanied by external atomic clocks for accurate time keeping (e.g. IGS, 2017b). Data used for corrections are broadcast over the internet in a standard format, via Networked Transport of RTCM via Internet Protocol (NTRIP) (Yan et al., 2009). It is also possible for these data to be downloaded after GNSS surveying, and post processed with the collected data to achieve similar results.

Differential GPS was once integral in circumventing selective availability to achieve sub 100m accuracy using the civilian code. Selective availability was an intentional degradation of the standard positioning service to limit the effectiveness of GPS devices used outside of US military operations. It was terminated May 1st, 2000, and modern satellites no longer have the functionality to reinstate it (GPS.gov, 2017).

2.1.4.2 Dual Frequency GPS

GNSS utilise several radio frequencies between 1 and 2 GHz, referred to as the L band. Standard GPS receivers currently utilise the L1 frequency C/A code. A pseudorange calculated from this code is accurate to several meters, while the carrier frequency can deliver accuracies of several millimetres (Eueler and Goad, 1991). In a device capable of receiving at least two frequencies, the dispersive nature of the ionosphere separates each frequency in proportion the length of time the wave travelled through the ionosphere (Groves, 2013). The final separation amount can be used to calculate the total length of ionosphere traversed, and hence the increase in range measurement, which can be adjusted accordingly.

2.1.4.3 Carrier Phase Positioning and Real Time Kinematic GPS

Current consumer GPS receivers utilise the timing and ephemeris data contained in the L1 C/A code (GPS.gov, 2017). Accuracy using this code alone is approximately 10-15 m, however this can

be enhanced to sub decimetre accuracies using GNSS augmentations satellites such as the American Wide Area Augmentation System (WAAS), or Japanese Quazi Zenith Satellite System (QZSS). Receivers operating on the C/A code use only the modulated PRN and navigation messages to determine satellite ranges. Advanced receivers can track the L1 carrier wave itself, with centimetre scale accuracy (Eueler and Goad, 1991). However, the repetitive waveform of the carrier wave leads to an ambiguity in matching the phase, which results in an integer multiple range error when the signal is incorrectly correlated. That is, the receiver is yet to determine exactly which period of the wave is the correct correlation. Integer ambiguity is only a problem when utilising carrier wave positioning and requires a second reference GPS to resolve. The second GPS determines the carrier phase offset at the satellite, and atmospheric delay and can also be utilised to provide a differential GPS measurement while resolving integer ambiguity (Groves, 2013). When carrier phase positioning is utilised with a moving receiver, it is termed Real-Time Kinematic, which is effective to around 20 km from the base station (ICSM, 2016). Figure 9 illustrates a complete differential RTK system.
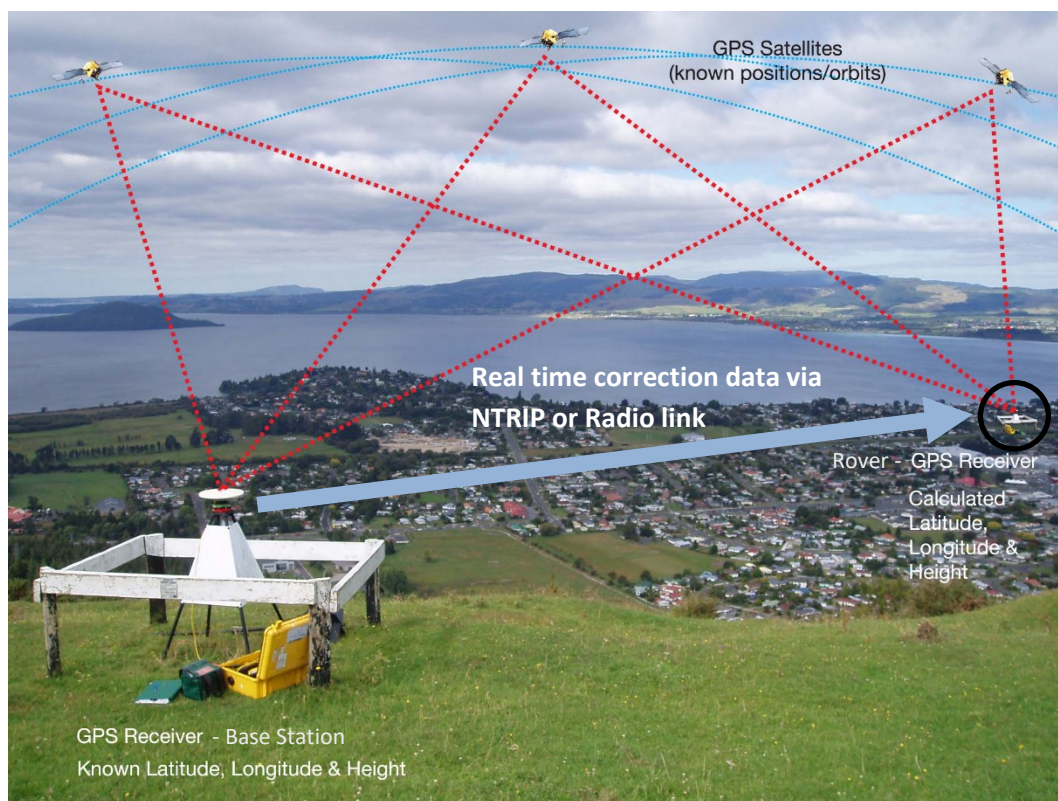

Figure 9 - Overview of a Differential, Real Time Kinematic GPS system

2.1.5 Near Future Advances:

GNSS are an important public and commercial resource, and are continually being upgraded by their respective authorities. GPS is currently undergoing modernisation with new satellites ready for launch before 2020 (GPS.gov, 2017). The frequencies and code broadcast by these satellites

are also revised and enhanced for modern usage scenarios. The L2C and L5 bands are both available, however are officially in pre-operational status and have limited consumer hardware support at present (GPS.gov, 2017). The GLONASS constellation is also continually upgrading satellites. In summary, the next decade will most likely show a transition from single frequency on the old L1 C/A signal to a multi-frequency GPS environment, as well as a doubling of the number of full constellations. Overall, sub metre accuracy is predicted to become typical on consumer hardware in the coming decades - driving a host of new applications, especially in the autonomous vehicle space.

2.2 The Kalman Filter

The Kalman filter is a widely used and thoroughly researched estimation algorithm used in smoothing and estimating system states. Originally developed by R.E Kalman (1960), the filter has been developed into many secondary mathematical products, including Rauch, Tung and Striebel's (1965) application of the Kalman filter to smoothing data. The filter itself has seen use across an immense range of applications, from spacecraft control to stock exchanges. It is also used in Global Navigation Satellite Systems, to combine ranging information from each satellite and return a best fit position. The Kalman filter is extensively covered in the literature, with overviews by Welch and Bishop (1997, 2006) and Grewal (2011). An overview of its application to GNSS is detailed by Groves (2013). A general introduction to the filter is presented here.

2.2.1 General Overview of the Kalman Filter

The Kalman filter is a simple, recursive mathematical process that integrates a model of the system process with measurements of the system's state. Control over the weight of the measured state is provided by the Kalman gain, which itself is computed as an estimate of the measurements' accuracy (Groves, 2013). As such, the Kalman filter combines a real measurement of a system with modelled expected behaviour of the system, with the estimated accuracy of each determining their respective weighting in the final output state. An overview of the process is shown in Figure 10, and is explained below.

The filter resolves in two component steps, a prediction step using the system model, and an update step using the measurements (Figure 10). The prediction step uses the known state (x_{k-1}) and state error (P^-_k) to predict the next state (x^-_k), using the model (A) and any known user input (B, u) (Welch & Bishop, 2006). The model is a predefined system of equations that describe the expected behaviour of the system between time steps. A simple positional model may describe
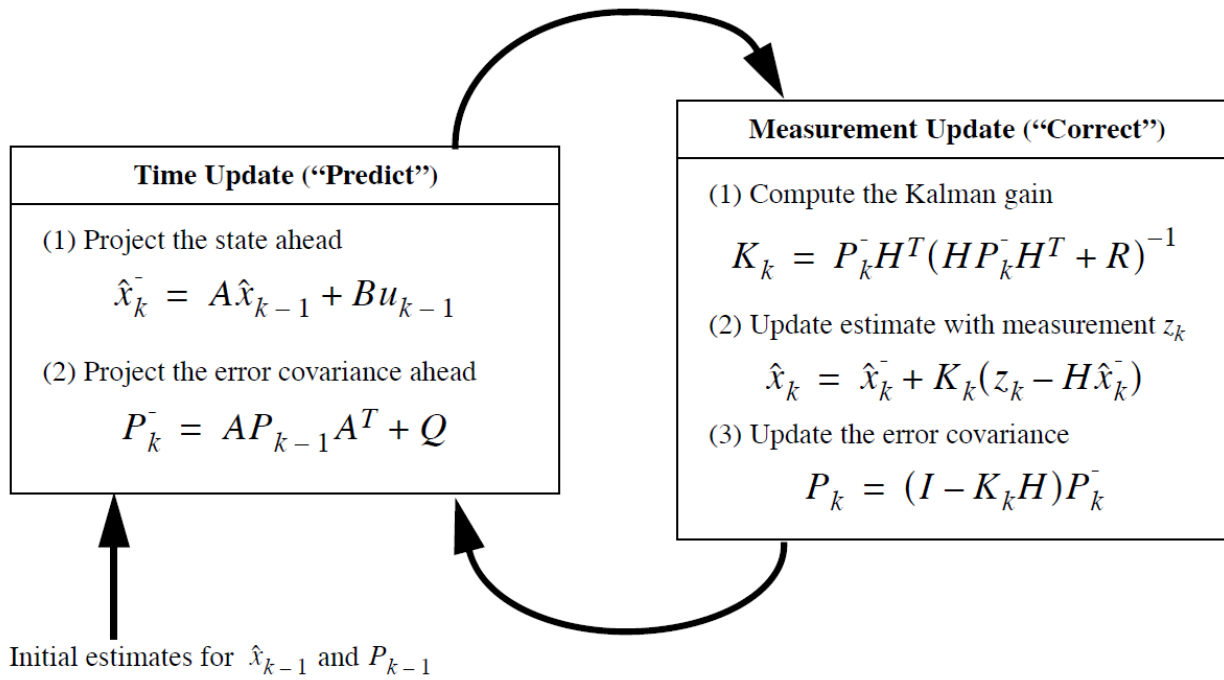
Time Update ("Predict")

(1) Project the state ahead

$$\hat{x}_k^- = A\hat{x}_{k-1} + Bu_{k-1}$$

(2) Project the error covariance ahead

$$P_k^- = AP_{k-1}A^T + Q$$

Measurement Update ("Correct")

(1) Compute the Kalman gain

$$K_k = P_k^- H^T (HP_k^- H^T + R)^{-1}$$

(2) Update estimate with measurement z_k

$$\hat{x}_k = \hat{x}_k^- + K_k(z_k - H\hat{x}_k^-)$$

(3) Update the error covariance

$$P_k = (I - K_k H)P_k^-$$

Initial estimates for $\hat{x}_{k-1}$ and P_{k-1}

Figure 10 – The two component steps to the Kalman filter. Welch and Bishop, 2006

that the predicted position will be the current position, plus the current velocity multiplied with the time step. The Q term is the process error, which represents the possible noise or uncertainty between steps (Groves, 2013). In rapidly changing systems, where it is possible the state varies greatly between updates, Q will be large, conversely in a subdued or well sampled system, the uncertainty between steps will be small. The state error covariance is used in estimating the Kalman gain (Welch & Bishop, 2006).

The predicted state and measured states are combined, scaled using the Kalman gain (K). The gain is updated during each iteration of the filter, using current state error (P_k^-) and measurement noise covariance (R_k) (Welch & Bishop, 2006). The measurement noise is generally taken to be Gaussian with a mean of 0, and covariance R_k, where R_k essentially describes the expected accuracy of each measurement. The Kalman gain is a simple ratio between the estimated error in the predicted state uncertainty, and the measurement uncertainty. It is then used to scale the corrections calculated from the measurements (z_k), which returns the output filtered state (x_k) (Welch & Bishop, 2006). The error covariance matrix is also updated, as a record of the certainty of the output state. Throughout these equations, H represents the observation matrix, a factor that translates state vector components into measurement components, and subscript k indicates the current update step (Welch & Bishop, 2006).

Following equation 1 of the measurement update (Figure 10), if the measurement noise covariance (R_k) is small, the Kalman gain approaches 1 and in equation 2 (Figure 10) the measurement dominates the final state solution. Conversely, if the measurement error is high, the Kalman gain will have a larger denominator, and the Kalman filter will minimise the measurement correction and rely on the predicted state, with the state error covariance remaining predominantly a product of the process error (Welch & Bishop, 2006).

2.2.2 Illustration of the Principle of the Kalman Filter

Faragher (2012) presents an easy to follow explanation of the Kalman filter following the principles of Probability Density Functions (PDF). A PDF is a simple measure of the distribution of possible states, with the maxima of the function the most probable state, and other probabilities detailed by their value within the function.
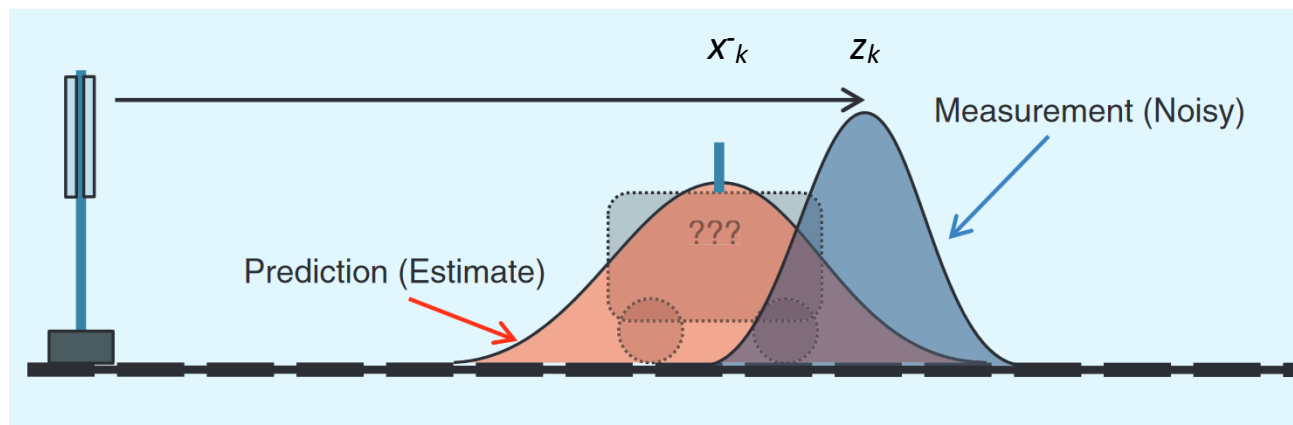

Figure 11 - Probability density functions of the prediction and measurements of a Kalman Filter application. Faragher (2012)

The example provided by Faragher (Figure 11) is that of a train moving on a one-dimensional track. There are uncertainties associated with both the measured position and the predicted position, indicated by the red and blue PDFs. The width of each function reflects their respective error matrices, while the maxima represents the state vector determined by each. If only measured values are considered, the train would be said to be located at z_k, and if only the prediction was used, at x^-_k. By multiplying the Gaussian PDFs we obtain an estimated state that integrates predictions and measurements, accounting for their respective uncertainties and returning a new best fit location, x_k, and associated uncertainty (Figure 12).
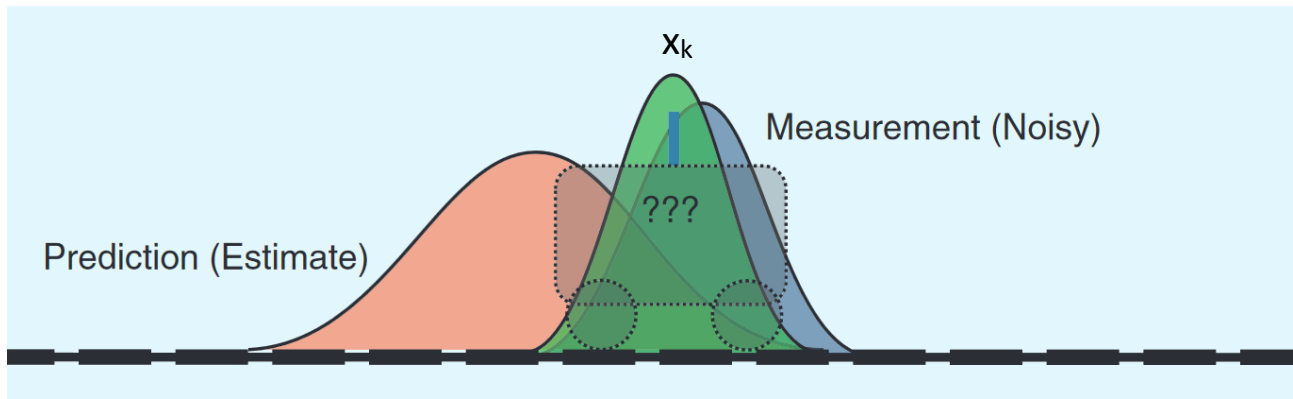
Figure 12 Estimated State (Green) probability density function. Faragher (2012)

2.2.3 Kalman Smoothing:

The original Kalman filter operates forward in time, upon the input of new measurements. However, it is possible for future states to be utilised as a constraint on present states, if the filter is being applied to a set of previously measured data. This is known as Kalman smoothing, of which there are two predominant methods (Groves, 2013); the forward-backward filter, and the Rauch, Tung, and Striebel (RTS) method (Rauch et al., 1965). The RTS method differs from the forward-backward computation by computing smoothed values on the reverse pass, as opposed to computing smoothed values from a combination of the forward and backward Kalman filtered states.

The forward-backward smoother, as shown in Groves (2013) simply combines a forward filtered solution from time *k* to time *k+t*, and a backward filtered solution starting from time *k* to time *k-t*. The two solutions are combined with weighting at each time interval according to their corresponding error covariance matrices.

The RTS method (Rauch et al., 1965) also calculates a forward Kalman filter, however at each interval the state and state error covariance matrices are recorded, along with the transition matrix. Working from the most recent measurement interval backwards, the current and previous error matrices are used in calculation of a weighting factor, termed smoothing gain, which in turn is used to combine the later, and current state estimates. This is subtly different to the use of Kalman gain for combining the predicted and measured states, in that the smoothing gain scales the two Kalman filtered state estimates based on their error matrices.

2.2.4 Pre-existing Application of the Kalman Filter to GNSS

Satellite navigation systems already utilise the Kalman filter in integrating satellite data and calculating position error before outputting a location fix. It may therefore seem pointless to undertake further Kalman filtering on the resulting location track. However, the information taken

into account during the Kalman filtering process is important – a GNSS receiver uses the Kalman filter to combine satellite ranges and previous estimations (Groves, 2013), while the implementation here combines previous positions and vehicle dynamics. By incorporating these data, a more precise GNSS track can be recovered.

The general Kalman filter presented in *Methodology* operates on linear functions only. An extension to it allows filtering of non-linear systems, and is known as the Extended Kalman filter (Groves, 2013). The system modelled here uses only linear equations, this the standard Kalman filter is sufficient.

2.3 Existing UAV Magnetometer Systems

Fluxgate magnetometers do not see as much use in geophysical surveying as proton procession sensors, due to their lower precision. However, the low sampling rate and bulk of proton procession magnetometers limits their applicability to lightweight aerial systems. For unlicensed use in Australia, an Unmanned Aerial Vehicle (or RPA) is limited to 2kg take-off weight (CASA, 2017). A brief summary of several current UAV-borne magnetic systems is presented here.

A fluxgate magnetometer system, was designed by Gavazzi et al. (2016) and flown with a 21 kg UAV (Figure 13), which successfully surveyed metallic pipe sections at 5m survey elevation. At 21 kg, operation of this drone requires certification for use in Australia.
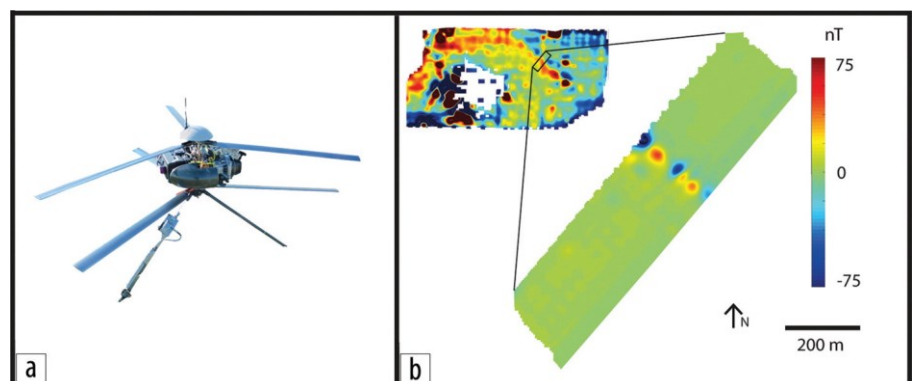

Figure 13 - Results from a calibrated fluxgate magnetometer system by Gavazzi et al., 2016. The UAV depicted (a) has an unloaded weight of 21kg, and the sensor system, 200g. The magnetic lineation presented (b) is due to a pipeline. The UAV was flown at 5m elevation.

Malehmir et al. (2017) constructed a 10 kg proton procession based UAV, with a flight time limited to 5 minutes for 2 km line distances. The proton procession magnetometer suffered from oversaturation, especially during take-off and landing, which is not a problem for fluxgates. While 2 km lines are acceptable for search applications, 5 minutes of flight with a rotation of 4 batteries from a diesel generator is sub-optimal for remote operation.

Wood et al. (2016) used twin caesium vapor magnetometers on board a 5 m, gasoline powered fixed wing aircraft with DGPS, and a take-off weight of 55 kg. This plane is designed as a

replacement for commercial airborne magnetic surveying, and is not suitable for the application investigated here.

2.4 Magnetic Sensing

There are several key points in outlining magnetic sensing. The first is the magnetic field component under investigation; in that it is possible to measure the Total Magnetic Intensity, or components of the field in defined directions. These are termed TMI and vector magnetics respectively. The second key point is the gradient; A magnetic field gradient is a measure of the change in magnetic field strength across a distance. It can be observed in situ, using two sensors separated over a known distance, or calculated using a single moving sensor. It is easiest to identify an anomalous magnetic source using a gradient measure, as large gradients arise from local sources, and the background field is generated by the Earth's core (Schmidt and Clark, 2006). Gradient sensors are also less affected by orientation changes, which are prevalent on aerial platforms and severely influence vector sensors (Schmidt and Clark, 2006).

The gradient method and vector magnetics can be used together to determine the gradient in two discrete frames of orientation – the direction between vector sensors, and the orientation of the sensors themselves. These can be described with the notation B_{xx}, where B represents the magnetic field, and the subscript defines the two orientation components in three dimensions: *x*, *y*, and *z*. Doll et al., 2006 found a vertical gradient measure outperformed total field products in their surveys, provided a low altitude (several metres) was used.

A gradient sensor is relatively immune to noise common to both sensors in the pair, as the strength of the field at each sensor will be of similar magnitudes. The target under investigation is more removed from one sensor in the pair during a survey, and thus the difference in field strength will be greater.

Chapter 3 - Methodology

This thesis aims to investigate the correction of GPS tracks, specifically with the intention of developing a lightweight geophysical RPA platform for meteorite recovery. There are four components to this research: the development and integration of a UAV-mounted RTK GPS system, the development of a gradient magnetometer sensor platform, the post-processing Kalman implementation on the positional data, and the integration of the magnetometer and aerial system. The development and testing of these components will be described here.

3.1 Hardware Design

3.1.1 Magnetic Gradiometer

The geophysical sensor used to trial location enhancements was an in-house fluxgate magnetometer gradiometer, utilising four Stefan Mayer Instruments FLC 100 Magnetic Field Sensors (Figure 14, Stefan Mayer Instruments, 2017) in a 1 m long linear array. The magnetometer output was read via an external Analogue to Digital Converter on the I2C interface of an Arduino Mega 2560 microcontroller, which simultaneously logged location from the Reach GPS over serial communication. Magnetic data was recorded as both raw signal and a Kalman filtered signal. Data were saved to a microSD card as a delimited list.
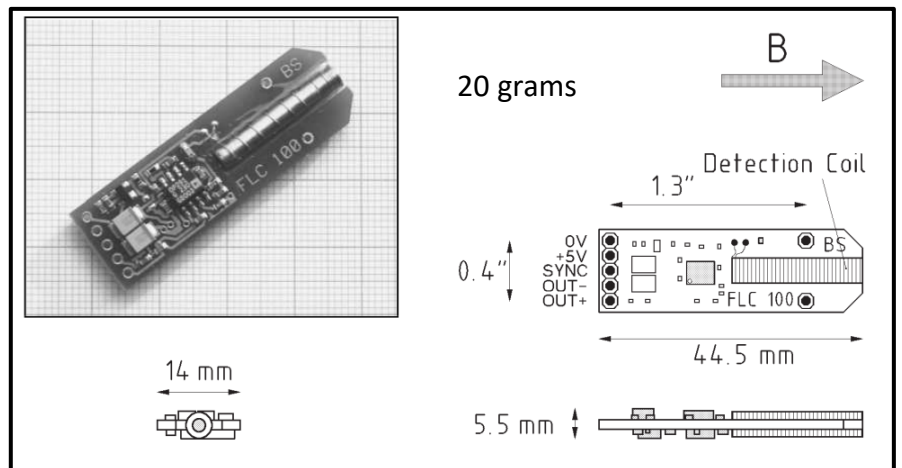

Figure 14 - Stefan Mayer Instruments FLC 100 Magnetometer

To make use of the magnetometers differential signal output and provide higher resolution sampling, an external ADC was used – the Microchip MCP324 (Microchip Technology Inc, 2017). This ADC offered selectable 12 to 18-bit resolution and an increased sample rate, as well as four differential inputs, which minimise common noise on the differential output of each magnetometer. The sensor differential output has a maximum range of 2.5 V, which required stepping down to the ADC input limit of 2.048 V, so a voltage divider was implemented. This was accounted for during scaling the sensor reading to magnetic units. At a resolution of 12 bits the

ADC can record accurate to 30 nT, which accommodates for the full sensor accuracy of 300 nT, and sensor noise which is specified at <0.5nT$_{RMS.}$

The sampling rate was limited by the Arduino code, and during initial surveys was tied to the GPS sample rate of 14 Hz. During the final testing, the GPS update was decoupled from the magnetometer readings, allowing the final magnetometer update rate to be typically 150 Hz. However, as GPS updates occurred at 14 Hz many of the magnetic readings required an interpolated position, which was provided after the Kalman filter process.

Noise was predicted to be a challenge for the magnetic sensor when positioned close to electric motors and other electronics, hence measures were taken to reduce its effect. Two lengths of shielded cables were run for the magnetometers, one for sensor power and magnetometer frequency sync, and the other for analogue signal. This minimised any electrically induced magnetic fields from within the sensor system and any induced voltage in the analogue lines from external magnetic fields. The ADC was placed as close as possible to the sensors to minimise the length of the analogue cabling. In this arrangement, significant noise should only be introduced by magnetic fields at each sensor. The array was mounted on a 1m length of carbon fibre, which is non-magnetic and lightweight. Shielded cables were run inside this length, terminating at the ADC and Arduino in the centre. Power was supplied to the Arduino by a USB power bank, and array power draw was less than 5 W.

3.1.2 Arduino Microcontroller

The magnetometer array and GPS were interfaced with an Arduino Mega 2560 microcontroller. This hardware allows for rapid development and a wide range of sensor integration methods. It used a 5 V power source, and supplied power to both the magnetometers and the Reach GNSS module. An onboard microSD card logged sensor and GPS readings. A Kalman filter implementation was implemented in real time on board the Arduino, in order to remove systematic and motor noise from for magnetometer readings. It was tuned to only filter highly variable noise, while retaining the change in response as the system moves over magnetic targets. While the SD storage served as the primary logging interface, data could also be transmitted in real time over USB connection, or through a pair of radio telemetry modules via Arduino serial and PC USB.

3.1.3 RTK DGPS System

The commercial Real Time Kinematic Differential GNSS system used was the Emlid Reach RTK GPS, henceforth referred to as the Reach. The Reach is an L1 C/A RTK Differential GNSS receiver, running on an Intel Edison control board (Figure 2). This means it utilises the public navigation data on the L1 band, carrier wave positioning, and can process correction broadcasts from a base station. The Reach was selected due to its low cost, size and weight, and an accessible design allowing easy integration with geophysical equipment. A pair of Reach modules can be utilised to implement differential GPS with corrections broadcast over radio link, or an alternative base station via NTRIP. The Reach module is relatively new hardware, released in 2015 into a growing market of cheap, miniature RTK capable devices. Comparisons with commercial RTK systems performed by other Reach receiver users find positions were within 5cm of survey grade products or GPS monuments (Wijnberg, 2016; Zeets, 2016). An investigation of the use of the Reach with UAV's found it provided centimetre accuracy in both static and dynamic tests (Eriksson, 2016).

To determine the optimal settings for flight recording several Reach settings were examined prior to performing trials.

First, to achieve the maximum 14 Hz location sampling rate the Reach was set to use only GPS and augmentation systems (QZSS, SBS). In this mode, there are still an average maximum of 15 satellites above 15° elevation (Figure 15) at the test site.
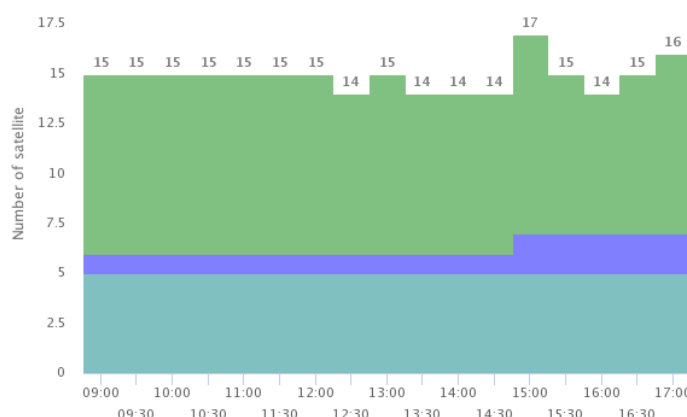

Figure 15 - Predicted GPS (Green), QZSS (Purple) and SBS (Aqua) satellites in view for an example day of May 1, 2017. Suzuki, 2014

Second, an account for Geoscience Australia's CORS network (Geoscience Australia, 2017) was obtained. This is a free network of internet connected base stations around Australia, with one such station located within 5 km of the university test site. There are other CORS networks in NSW, however they are commercially operated. Corrections broadcast by CORS stations can be utilised by the Reach over the internet, and offer enhanced accuracy. The AUSCORS network provides correction data at 1 Hz for all supported constellations (Geoscience Australia, 2017). In situations where no internet or station is available, the second Reach module can be used as a correction broadcaster. When creating a base station, the Reach's static position is averaged over a length of time and saved as the base station co-ordinate. In this mode corrections are broadcast from the base station via serial radio

telemetry module. The radio transmitters utilised during testing had an effective range of 200m, however radios are available with ranges beyond the 10km effective range of RTK, or the use of the cellular network is possible (Emlid, 2017).

Finally, to utilise the Reach with the Arduino sensor platform the location data are output as a text string over a serial connection. Several methods of logging these data were investigated, including NMEA formatted sentences. Of the different methods, a single location string per fix update was chosen for ease of code integration and performance, as it did not require the decoding of NMEA sentences or computationally expensive mathematical operations, increasing magnetometer sample rate. Operation of the differential receiver during field work will be described in the following sections.

3.1.4 Log Structure and Data Preparation

The logfile format underwent several revisions throughout system design, however the basic structure was retained. The file was a space delimited list of both raw and Kalman filtered magnetometer readings for each sensor, followed by position information. In NMEA mode, these were selected as: Latitude, Longitude Altitude, Date, Time, Satellites in View, GPS status (Single or DGPS modes), Velocity, and Heading. In single string mode, a single line of Date, Time, Latitude, Longitude, Altitude, Satellites in view, Status and positional accuracy information was recorded. Each row of the log corresponded to a single sample point.

3.1.5 RPA Platform

Two Remotely Piloted Aircraft systems were constructed during this thesis. The first was an off the shelf DJI Phantom 3 Professional (RPA weight – 1280 g). The second was an Ardupilot (ArduPilot, 2016) based custom system constructed by the author (RPA weight – 1300 g). In both systems, the sensor system was mounted independent from the RPA electrical system, with the exception of the RTK GPS, which could be used as the positioning device for the custom drone. As an off-the-shelf photography drone the Phantom 3 (Figure 16) was poorly suited to mounting the sensor suite. A plate compatible with the existing mount for the DJI camera was designed and 3D printed to securely attach the magnetometer array to the airframe, with the DJI camera removed. However, the magnetometers, which were positioned within 20 cm of the electric motors were likely to cause magnetic and electrical interference. The GPS could not be integrated with the DJI flight controller due to the closed nature of the system, and the only optimal mounting point for the Emlid Reach antenna degraded the performance of the onboard GPS used for guidance by

blocking satellite reception to the onboard GPS. Motor performance and stability were good, and the system achieved a flight time of approximately 15 minutes. All flights were performed manually because it was not possible to create and fly autonomous flight paths prior to take off.

Figure 16 - Magnetic Gradiometer Array on board the DJI Phantom Pro 3. The circular ground plane, centre, was required to be smaller for propeller clearance on the DJI, at 8cm diameter.

The custom Ardupilot based quadcopter (Figure 17) was much more suited to the development of a geophysical platform, due to its open source hardware and software. The flight controller was highly configurable and had pre-existing software integration with the Reach GPS, and natively supported base station correction data transfer over standard RPA radio communication. A computer program or mobile application could control and monitor the RPA in real time, as well as pre-plan flight paths and allow autonomous flight. The airframe chosen allowed positioning of the magnetometers further from the motors, however they remained close (50 cm approx.). Development of the custom drone began late in the project and was not completed in time for field testing. It is presented here as a proof of concept for a comparable, more open system with accessible hardware and software which allows improved design and implementation of the magnetometer system. Several flights were performed carrying the magnetometer array, however time did not permit final tuning of the system to achieve satisfactory survey performance.

A complete system diagram is presented in Figure 18. In this system, a radio transmitter can stream observations and flight data in real time to a PC or mobile device, allowing on the fly data quality control.

Figure 17 - Custom UAV with Reach GPS module present. The copper groundplane (15x15cm) is prominently featured beneath the GPS antenna in the centre image, and blocks electic interferance from the flight control system. The Reach GPS can be used for UAV navigation as well as data sample positioning. The magnetic gradiometer system mounts easily to two service rails running the length of the frame, or could be attached to a suspended gimbal.
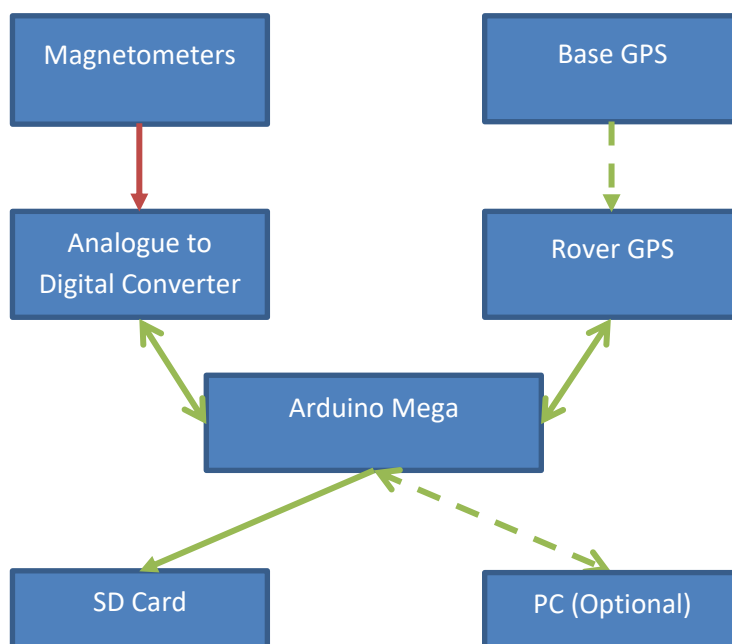

Figure 18 - System diagram. Red indicates analogue signals, green digital, and dashed indicates radio link.

3.2 Field Surveys

A total of two full field surveys were conducted to test system operation. The first took place on the campus grounds with a walked gradient array, tested against a commercial proton procession magnetometer. The second survey was conducted at a local sports field to test the full RPA system performance with simulated magnetic targets including an 1107g sample of the Wolfe Creek iron meteorite.

3.2.1 First Trial – University Grounds

On the 11th April 2017, an on-campus trial of the positioning and magnetometer array was performed, using a walked survey over the campus grounds in the location of a known drainage culvert. For comparison, a commercial Proton Precession magnetometer was used to survey the same area. A 20 m by 20 m grid was marked with survey tapes, centred above the surface expression of the culvert. Figure 19 shows the locality on Google Earth™, with the taped extent overlain. It is important to note that due to projection and datum errors, Google Earth™ imagery can be incorrectly located, sometimes by up to 10 m. The overlays presented here have been positioned per their recorded
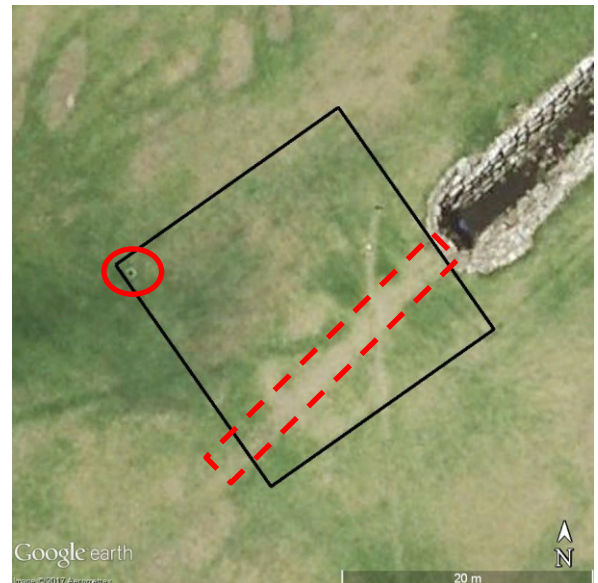

Figure 19 – Approximate Location of Culvert grid area (Dashed outline), Macquarie University grounds. An exposed metal drain is present in the West corner (Circled).

co-ordinates, and then shifted to account for these errors where necessary. The base image was chosen as the highest resolution image which also shows the surface expression of the culvert. There is a gentle upward slope in each direction perpendicular to the culvert.

The aim of the culvert survey was to conduct the first formal field test of the system, specifically the set up and operation of the RTK positioning system (including optional follow up GNSS post processing), and the magnetometer array performance. The commercial RTK GPS system has advertised centimetric accuracy, which is likely to exceed the accuracy of the taped grid. The positioning test was therefore designed to provide example location data to develop the Kalman filter, and not as a performance test for the Reach module. The magnetometer gradiometer was tested against a commercial Proton Precession magnetometer.

The magnetometer array was initially walked in the Bxy orientation, followed by a Bxz orientation. In the Bxy orientation, the array was horizontal with sensing axes perpendicular to the array, and walked at waist height. In the Bxz orientation, axes were perpendicular to the array, which was held vertical with the lowest magnetometer just above the ground. It should be noted in the Bxz configuration the GPS antenna was located poorly, with the antenna's ground plane positioned with the plane facing horizontal, giving quite poor satellite reception and increased ground multipath effect. This is seen in the position log (Figure 21) as a very erratic location path.

These poor GPS data were used for worst-case scenario investigation. Lines were walked NW-SE at 1 m spacing for both gradient surveys. Data were acquired continuously at 14 Hz with a regular walking pace. The gradient measurement is less affected by orientation changes than single vector magnetometers, however consistent field measurements from individual sensors were desired during testing, and as such the array was limited to approx. 20° of rotation. The proton precession survey was performed with 2 m line spacing, and a 1 m sample interval along each NW-SE line. The magnetometer was placed level on the ground, oriented North during readings. Unlike the gradient array, a rest and read period of several seconds was required at each point, meaning acquisition was much slower. Sample locations are tied to the accuracy of the located tape grid, as opposed to measurements being recorded with the location and accuracy provided by Differential GPS. The Emlid Reach RTK GPS module was used in differential mode, with corrections provided by a local NTRIP broadcaster over LTE internet connection. The correction provider was site SYDN7, a permanent installation operated by Geoscience Australia (Geoscience Australia, 2017) at the National Measurement Institute, 6km East of the survey site. The close proximity to a Continually Operating Reference Station (CORS) is atypical for most field work, however it provided an opportunity to test GPS performance while using a very close correction provider.

Figure 20 and Figure 21 show the post-processed ground tracks of both gradiometer surveys, in single and differential GPS modes. These plots were generated from the same recorded satellite observations, however the red solution does not incorporate corrections (single mode). Green (fix) and yellow (float) reflect differential operation, with green indicating the best fit solution is greater than 3 times more likely than the next best solution.

As seen in Figure 20 the differential GPS easily reconstructs the 1 m spaced lines during the horizontal survey (Figure 20), and presents a recognisable track in the vertical survey. The single mode track during the horizontal survey reconstructs the walked lines fairly well at times, however the poor mounting solution in the vertical survey (Figure 21) completely obfuscates the walked track in the single mode observations. These data will present challenging tests for Kalman filtering.
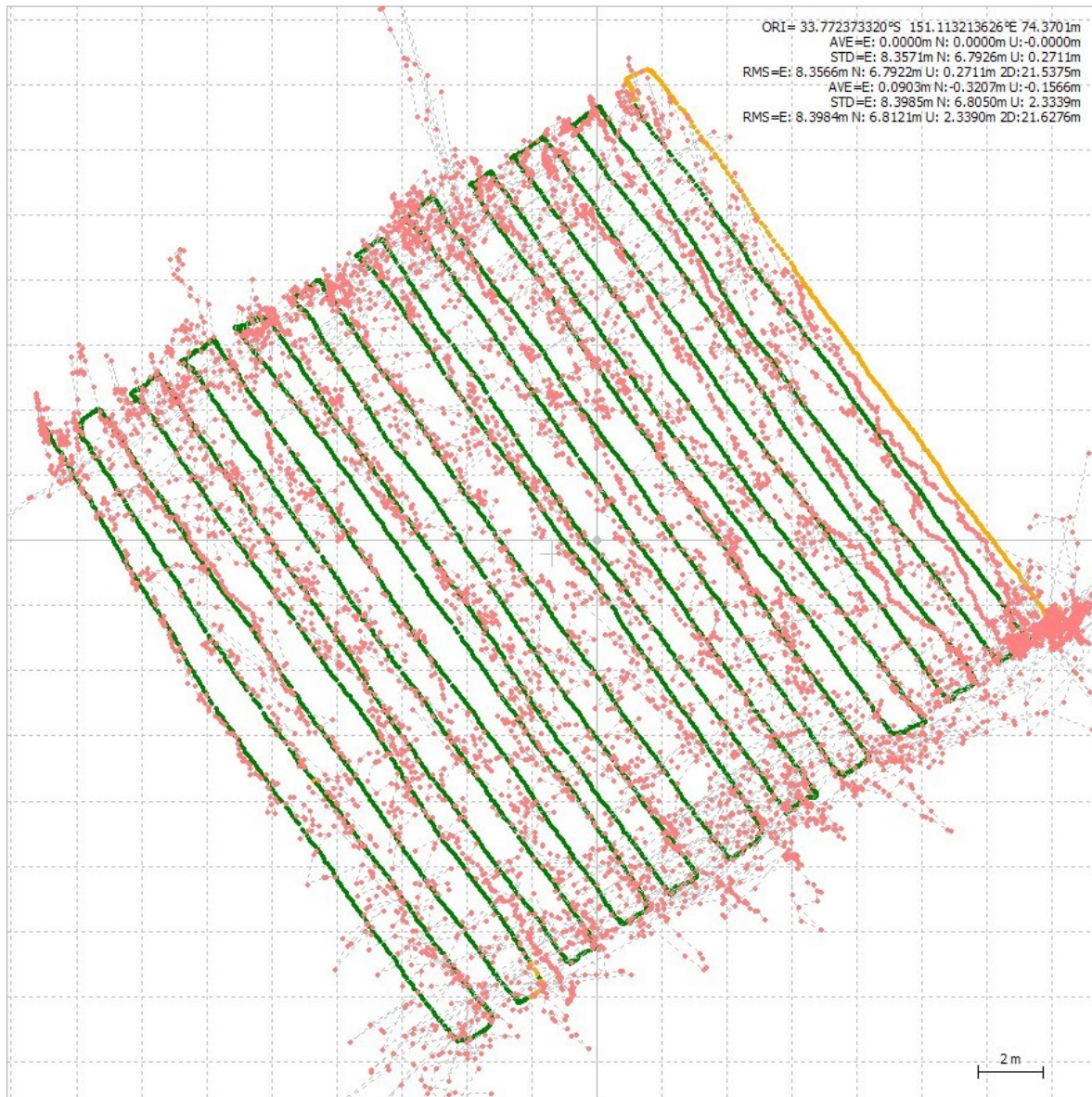

Figure 20 - Single (Red) vs Differential (Green/Yellow) ground tracks for Horizontal survey. North up. Single and Differential mode data acquired simultaneously. There is a vague appearance of a walked grid survey in the single mode data.

The proton precession magnetometer data and input station positions were recorded on the system's inbuilt storage and downloaded to a PC. These were imported to Python 2.7 for plotting and processing, before a final grid in Generic Mapping Tools 4 (Wessel and Smith, 1998). In Python, a copy of the data was normalised such that points outside of one standard deviation were reduced in magnitude, retaining the structure of the magnetic anomaly but allowing finer detail to remain.
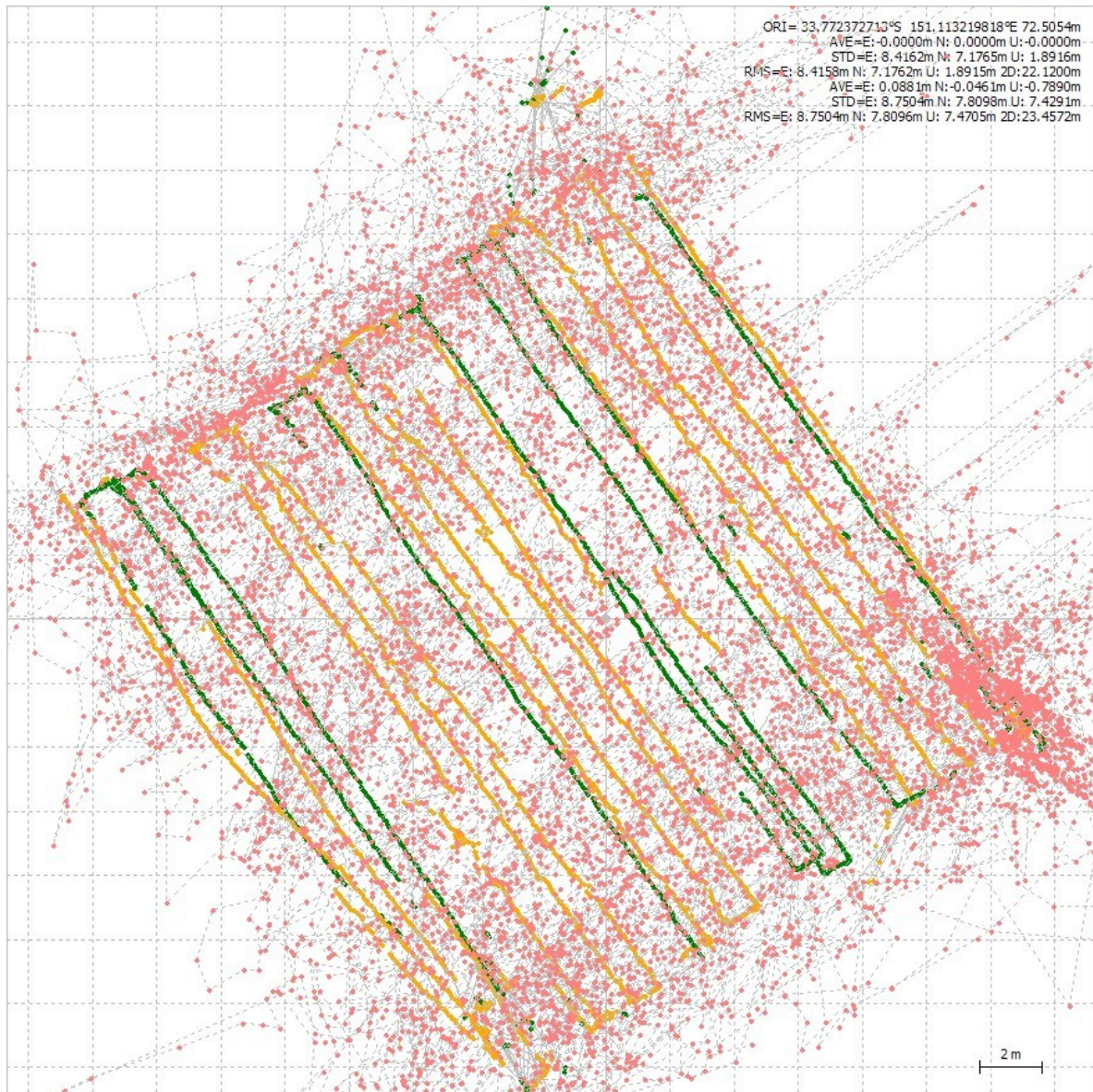

Figure 21 - Single (red) vs Differential (Green/Yellow) ground track for Vertical (poor reception) survey. North up. No regular grid pattern is observable in the single mode track.

The gradient data were recorded by the Arduino mega onto a microSD card, which was read by a PC. The 3D position, time, number of satellites and fix status, as well as raw and Kalman filtered magnetometer readings were recorded as a delimited text file. These were imported to Python for

processing. In this field trial magnetic readings and position information was synchronous at 14 Hz so no work was required to interpolate positions for the magnetic data.

The Kalman filter implementation as described above incorporates velocity, time and position information to determine the most likely state (location) at any given time. Position and time were recorded by the GPS, while velocity and heading are geometrical products calculated from the previous positions. The velocity at each position record was calculated as the change in position divided by the time elapsed between measurements. The resulting velocity was filtered with a moving average filter, that took into account the past 4 measurements.

3.2.2 Second Trial – Sports Field

A second field survey was conducted on the 29th August 2017, and repeated on the 11th September after it was discovered the recorded sample locations had been corrupted. Both surveys were conducted in the same manner and with identical aims, which was to investigate the flight characteristics of the system. To this end, several flights were conducted, followed by walking of the same approximate lines while carrying the RPA system. Two surveys were walked for comparison between the electrically and dynamically noisy flights and a more stable carried platform. System operation was identical other than the power state of the UAV. The test ground for this survey was a local sports field (Figure 22), and the magnetic targets used were magnets and the same 1107 g iron meteorite sample as previously used. Field lighting and power distribution were noted around the perimeter of the field, as well as an in-ground irrigation system, which may exhibit a magnetic response. Also present are metal goal posts and discus nets, which may cause a large magnetic response.
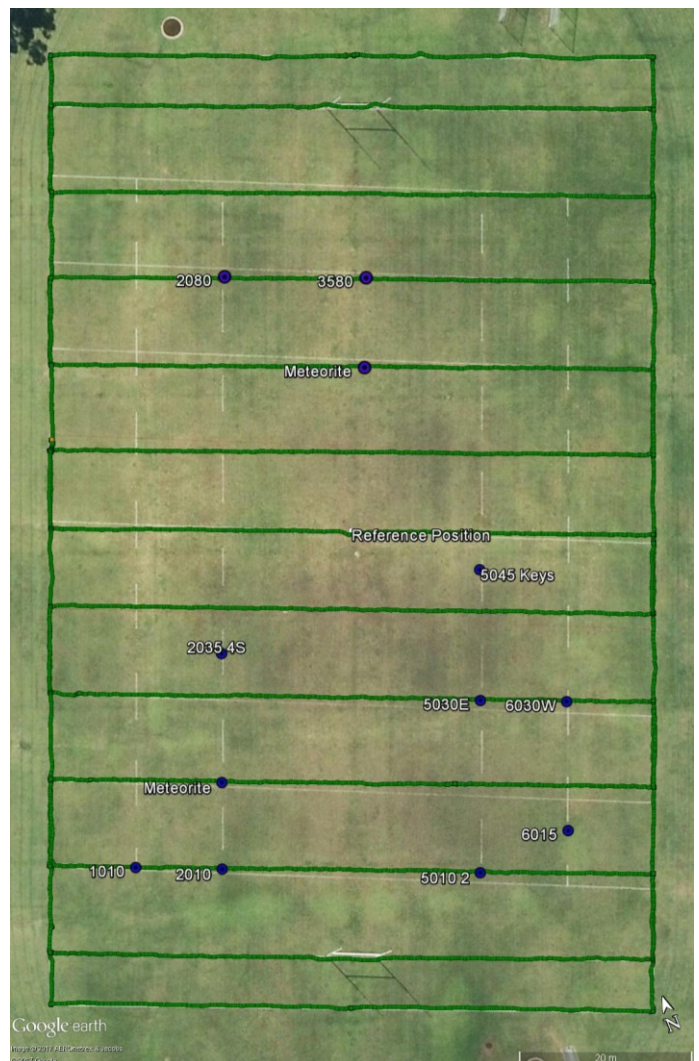

Figure 22 - Sports Field survey area. Note base imagery is correctly located, however the field lines are painted askew. Imagery date 2014. Green lines indicate the GPS recorded current field markings, blue points indicate the surveyed positions of targets. The 50 m centre line was the division between North and South surveys.

Unlike the previous survey on the campus grounds, no CORS station was within range for real time kinematic GNSS operation. The nearest station was SYDN7, used previously but now 65 km to the South. It was still possible to use this correction provider, but at reduced accuracy and a lower rate of achieving Fix DGPS status. This necessitated the use of two Reach GPS modules; one was erected at the centre of the field above a marked point (e.g., Figure 23) and the other was used during surveying. The stationary GPS recorded one hour of GPS, Galileo, Beidou and QZSS satellite observations as well as corrections broadcast by the SYDN7 CORS. Despite the distance, enough satellites were common to SYDN7 and the Reach unit to often achieve Fix status. The average Fix position recorded during the 1-hour operation was then saved as the base station location at the marked survey point at the centre of the field. This receiver then became the base station for the rover, and the two were linked by 915 MHz telemetry radio for surveying.

Figure 23 - Reach local base station above survey mark. The base station was moved to the central field during later tests due to poor sky view at this location.

During line surveying and target positioning, the rover GPS module used GPS, Beidou, QZSS and Galileo satellites. The module was installed on a 2 m high pole to achieve greater sky view and minimise multipath from ground features. Points were recorded as the average position over 30 seconds of fix status at each point. Each side line and meter line intersection of the field was located, and then the GPS was walked tracing the line markings to produce the track shown in Figure 22, after minimal post processing. While surveying the GPS antenna was attached to the top of the DJI Phantom 3, with ground plane above the drone's motor and flight controller noise plane. A smaller, 8 cm diameter ground plane was used for space constraints, and to retain functionality of the DJI's onboard navigation. To attain the maximum 14 Hz update rate of the Reach GPS module, only GPS, QZSS and SBAS could be utilised on the rover.

The field was split into North and South halves to allow for the RPA's 15-minute flight time. The fields 50 m line was also the location of the base station, where satellite coverage was greatest, and as such the 50 m line was not covered by either flight. Tapes were lain at 10 m intervals across each half of the field to determine line spacings and provide target positions and names. The targets were 5x5x5 mm cubic rare earth magnets, aligned with their magnetic north pole facing

grid north, parallel to the field side line. This was recorded as it is possible to observe the direction of magnetic dipoles in magnetic profiles, so a recorded orientation would increase detection confidence. One iron meteorite sample was also presented, and in the Northern field, magnets were grouped to present a larger response.

Flights were performed at an average elevation of 0.5 m, following earlier tests determining the magnetometers could detect the meteorite up to 0.6 m, and maintaining a safe flight height. The magnetic targets could be sensed beyond 2 m, and would serve as additional testing targets. Due to flight controller limitations of the DJI drone, flights were flown manually, using the on-board visual and satellite assistance. To limit orientation changes of the array, no yaw commands were issued, and banking (in the axis perpendicular to the array axis) input was kept to a minimum. This meant however that any course corrections to account for crosswind or autopilot input took longer to complete. The pitch axis of the RPA was parallel to the sensors, meaning only a minimal change in elevation and orientation was presented to them. Both tests were flown on calm days, but the occasional breeze meant some flight lines were not entirely kept above the desired line. However, line spacings and survey area were consistent between walked and flown surveys. The magnetometer array was walked and flown in the Byy configuration, with lines perpendicular to the early North-South sideline of the sports field, meaning the sensors were aligned approximately North-South. Data were recorded from take-off through to landing, so some initial and final points are removed during post processing to remove altitude and non-survey track effects.

3.3 Post Processing

3.3.1 GNSS Post Processing

An optional step for real time kinematic GNSS surveying is post processing, which is performed to increase the accuracy and duration of fix status of a survey using the observations and corrections recorded by the receiver. Emlid uses the open source RTKLIB (Takasu and Yasuda, 2009) for both the Reach receiver and post processing capability. With this software it is possible to reconstruct receiver position from raw satellite observations, as well as incorporate additional data such as base station corrections, IGS measured ephemeris data, and atmospheric models. Providing these additional constraints can both improve the accuracy of fixes, and provide a greater number of "Fix" status positions than field based RTK recordings. This was undertaken with the field recorded data to provide single mode and differential mode position logs for the same recorded observations.

3.3.2 Logfile Processing

Data were processed in Python 2.7. In all tests the raw Arduino logfiles were structured into arrays for processing. Pre-processing included calculation of the time interval between points from the recorded GPS time, and velocity by averaging the distance over time for the previous 4 points. For the sports field tests, GPS positions were asynchronous and slower than magnetic readings, and as such missing positions required position interpolation. The Kalman filtered points were linearly interpolated, and the intermediate positions supplied to magnetic data with missing positions. That is, linear interpolation to supply magnetic readings missing location data was performed after removing noise from the position tracks.

It was discovered the default post processed positions from the Reach observations did not record the exact same observation times as the Arduino position log. There were often positions recorded in one but not the other, or at a different time interval. To overcome this, only the observation data in the same exact time window as the Arduino log were processed, and output with a common initial time. This ensured every Arduino logged position had a corresponding single mode observation position. The single mode latitude and longitude were then written over their time corresponding field data positions. These were then filtered and plotted following the described process.

Generic Mapping Tools 4 (Wessel and Smith, 1998) was used to plot magnetic data. Due to the high density of samples, GMT's blockmean function was used to obtain a uniform grid of average values across the survey area. The increments for these functions varied between $1\text{x}10^{-4}$ and $1\text{x}10^{-6}$, with coarser increments used in the faster, flying surveys.

3.3.3 Kalman Filter Implementation

The Kalman filter was designed to track x position, y position, x velocity and y velocity. No control input measurements could be supplied to do the closed software of the DJI drone. The system of equations for state prediction are detailed in the below equations. Each term in the process uncertainty matrix, *Q*, was scaled by *dt*. The filter was otherwise implemented as described above.

$$x_k = x_{k-1} + v_x*dt$$

$$y_k = y_{k-1} + v_y*dt$$

$$v_{x,k} = v_{x,k}$$

$$v_{y,k} = v_{y,k}$$

Equations – System model for the Kalman filter

Chapter 4 - Results

Two formal field surveys were conducted during this research. The first tested the precision positioning capability and magnetic gradiometer performance of the system. This was performed on campus as a set of ground surveys. The second was performed at a local field, where the aerial system was tested against walked surveys. Positioning data from all surveys are processed with the Kalman filter, and observations on the filter performance will be presented.

4.1 Kalman Filter Testing

Each implementation of a Kalman filter must be tuned for the system it performs in. Other than creating the system model and defining input measurements, this is done by adjusting values for the error matrices, specifically the measurement error and system error covariance matrices (R, Q). These matrices represent the level of noise or uncertainty in the measurement (R), and in the system over time (Q) respectively. It is also possible to tune P, the initial uncertainty, however as measured positions are available from the initial survey record, it is unnecessary to tune P for this implementation. The Kalman filter for these surveys incorporated a calculated average velocity from position data, as described in *Methodology*.

Investigation and selection of optimal parameters for the measurement error, R, and system error, Q, are presented here. Selection of each was performed by inspecting the resulting path smoothing on field survey positions and the mean velocity for the previous four points.

The measurement error, R details the uncertainty due to measurement noise. Values shown here are elements of a diagonal matrix, which allow each measurement in the system to have its own associated uncertainty. System error, Q, is input similar to R as a diagonal matrix, however this is then scaled by the time difference from the previous iteration. In this manner, an increased time gap between measurements increases the uncertainty of the returned positions. The identity matrix is used to prescribe individual uncertainties for each process, that is for each equation in the modelled system.

Comparisons between filter results for these different error inputs are shown in the following figures (24-26). The data used are field recorded differential positions from the horizontal gradient culvert survey. Figure 24 (Left) shows the smoothing effect as the measurement covariance matrix, R, grows smaller, and the measurement is trusted less.
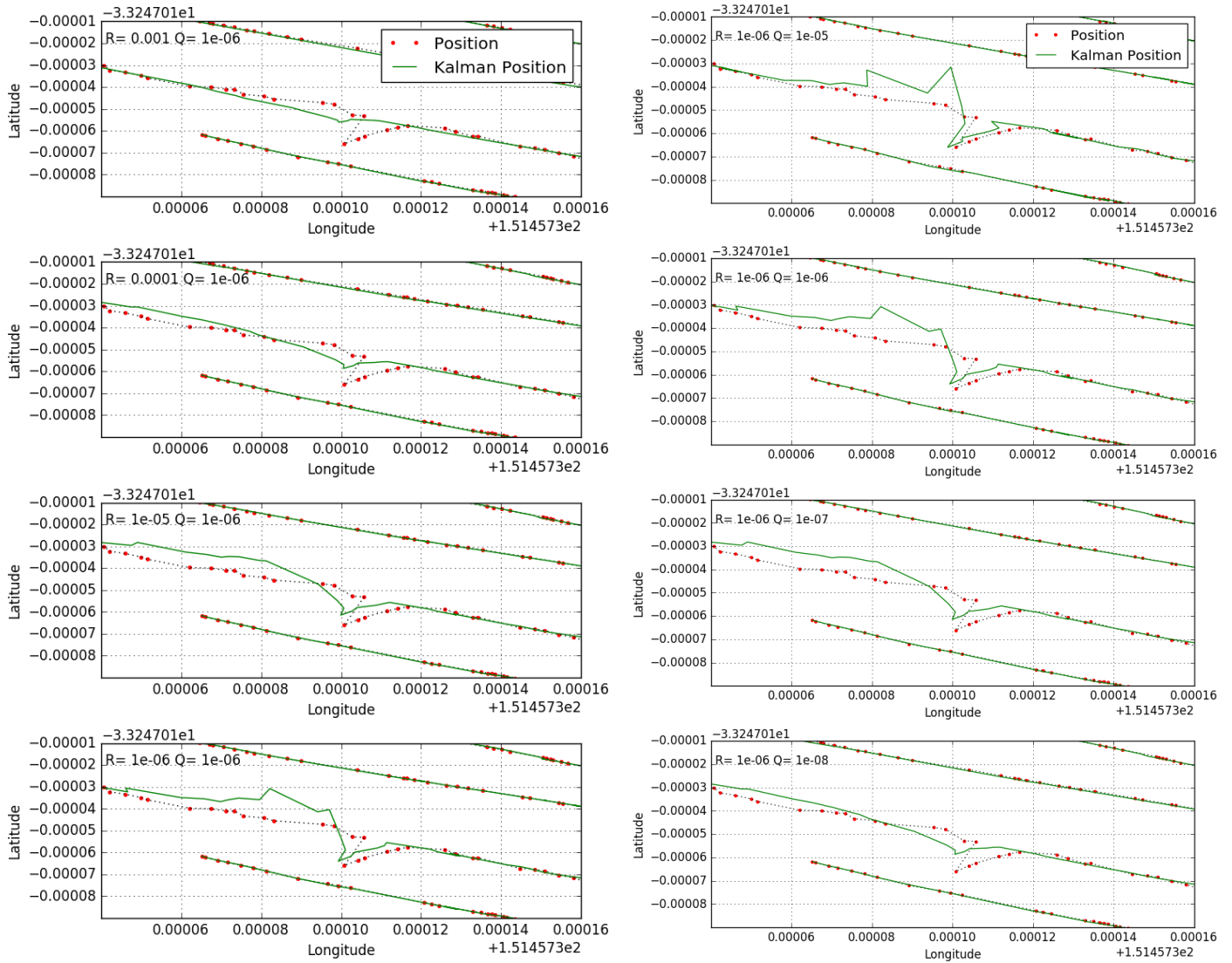
Figure 24 - Effect of R (Left Column) and Q (Right Column) on smoothing performance for data collected of the North Walked Field Survey. Red circles indicate recorded field differential positions, while the green line indicates the Kalman filter results. Values for Q and R used are detailed as text within the figure for each subplot.

Figure 24 (Right) shows the system error covariance matrix, *Q*, as it grows smaller and the uncertainty between measurements is lowered. Note 1×10^{-6} is used as an intermediate value to test against in each plot. It is apparent there is no one best choice based on these data. However, observing the filtered velocities (Figure 25) can assist in selection.

While R=1×10^{-3} and Q=1×10^{-6} seem acceptable from observing the location data, it is seen in the velocity data (Figure 25, Left) these values return poor filtered velocities. Hence, R=1×10^{-6} and Q=1×10^{-8} were chosen as the filter parameters, due to their good performance in smoothing both position and velocity. Ideally, R reflects the square of the measurement uncertainty, which for the GNSS system used here would equate to values of approximately 1×10^{-4}. Finally, it is important to note the smoothing effects on the line corners. Several values of Q are shown (with R = 1×10^{-5}) in Figure 26, and as Q grows smaller the corner fit is decreased. While excessive smoothing should be avoided, position fit in this application during cornering manoeuvres are likely to have additional magnetic noise and irrelevance to the grid area. Thus, it is acceptable to sacrifice corner fit for

improved line fit. Including heading and velocity measurements in the Kalman filter in future will account for this, as the filter will include the control inputs in the prediction component. These will inform the filter that the craft will be cornering, and as such the filter will not minimise the motion.
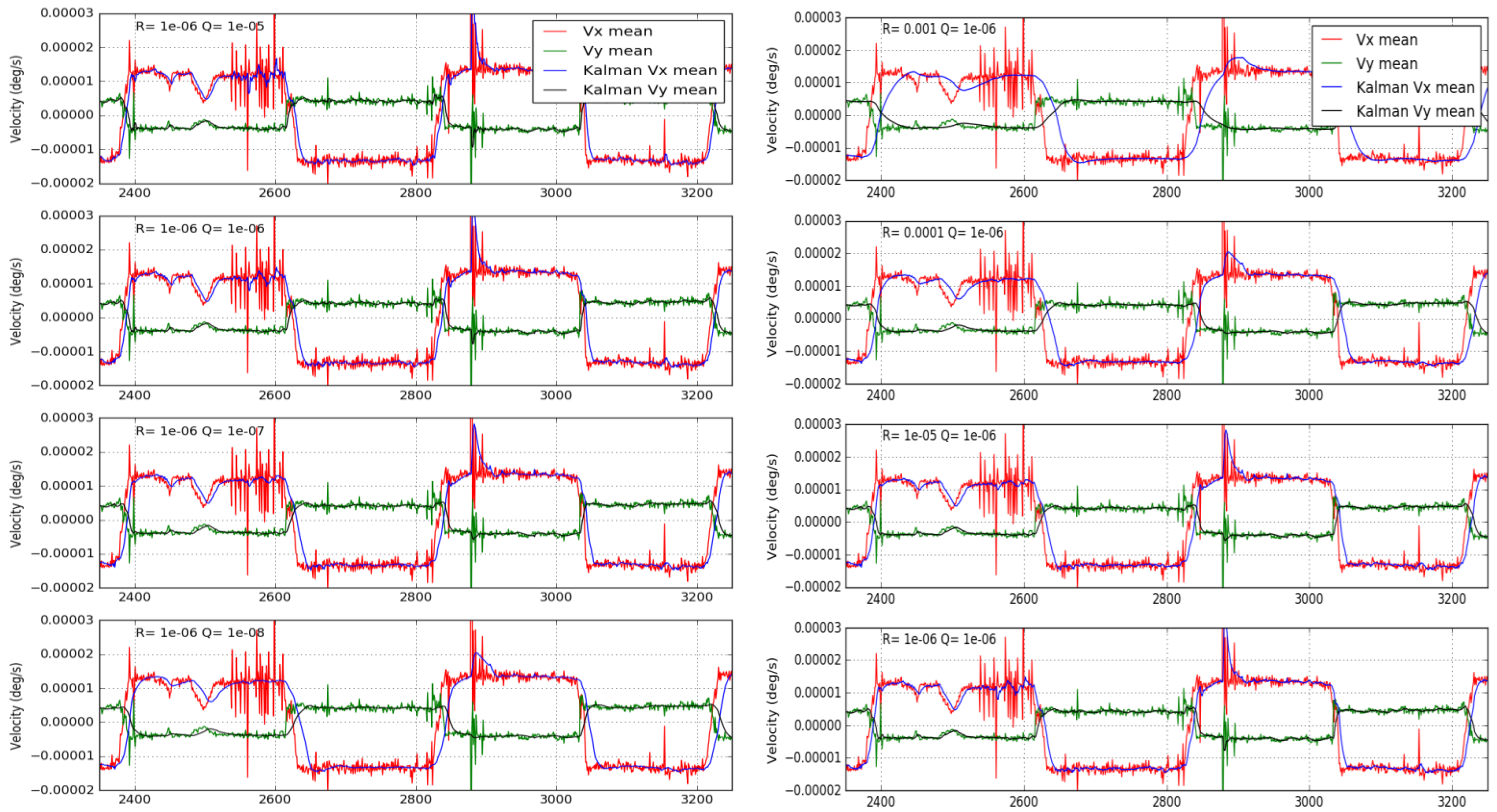

Figure 25 - Effect of R (Left Column) and Q (Right Column) on latitudinal and longitudinal velocities. A section of the full velocity record from the Northern Sports Field Survey is shown for brevity. Mean velocities are a moving average filter taking into account the previous 4 measurements.

4.2 Field Surveys

Each survey has positions recorded directly from the receiver during surveying (noted as "Raw GPS"), as well as post-processed single mode (noted as "Single Mode") and post-processed differential mode logs. Using a base station during surveying allowed the recording of differential positions in real time to the Arduino data log. As described in *Methodology*, the post processed results are made using the same satellite observations as recorded in the field during the survey, but without the differential corrections. These post processed positions will demonstrate
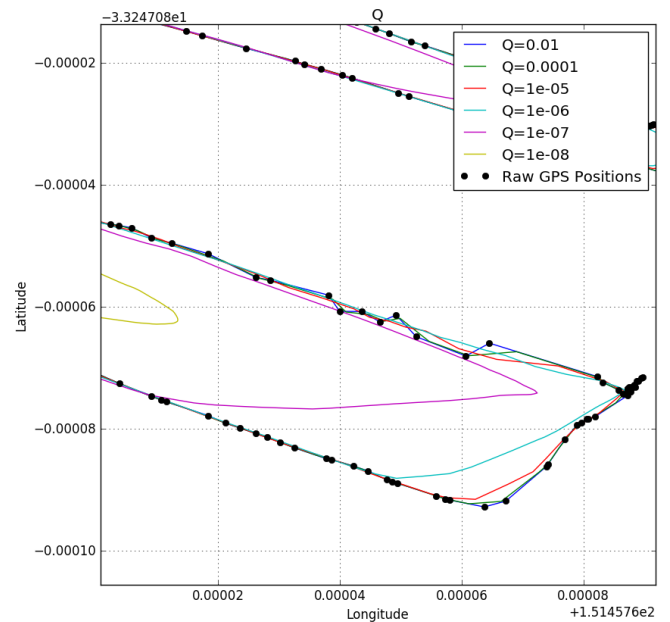

Figure 26 - Corner effects when excessive error values are used.

4-35

the enhanced precision and accuracy made available using differential corrections, and allow investigation of Kalman filter performance in this application. Finally, magnetic data recorded for each survey system will be presented.

4.3 Culvert Field Test

The culvert field test was performed above a known drainage culvert on campus. Two surveys were performed with the gradiometer array, the first with a horizontal gradient and the second with a vertical gradient. A third survey was performed with a proton precession magnetometer, for comparison with the gradiometer magnetics. Figure 27 shows the approximate extent of the surveys.
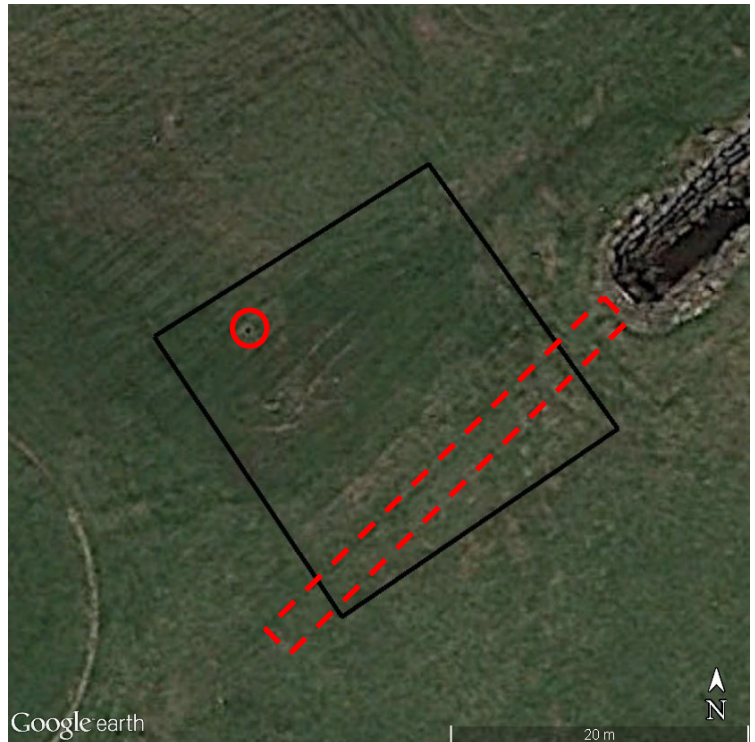

Figure 27 - Survey outline, with culvert outlined in red and drain circled. Figure 19 Shows the extent of the culvert, and as a comparison to show the inaccuracy between different historical imagery layers of Google Earth™.

4.3.1 Horizontal Gradient

The horizontal gradient was measured by the array of four fluxgate magnetometers, with the array held approximately horizontal and the magnetometer sensing axes perpendicular in By. The GPS antenna in this orientation had a clear sky view. For both culvert surveys, the base station used for differential corrections was the *SYDN7* AUSCORS site, 6 km to the East. Survey area is shown as the black polygon in Figure 27.

4.3.1.1 Field Recorded GPS – Horizontal Gradient

The field differential GPS trail recorded by the walked horizontal survey above the
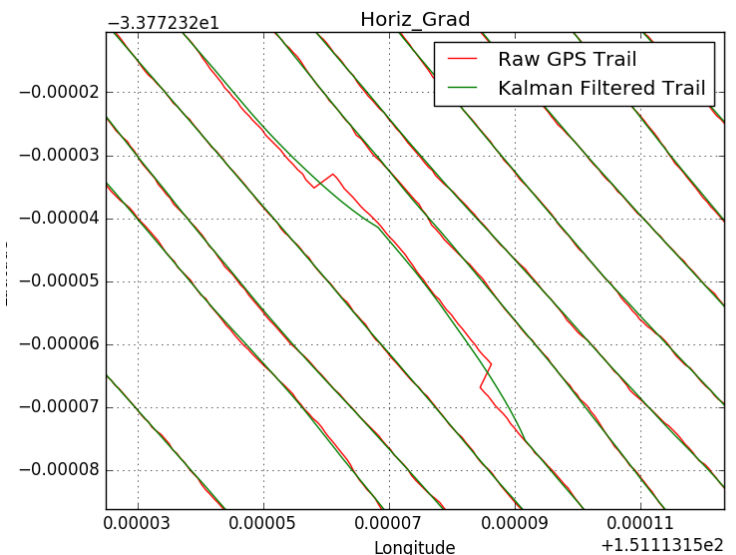

Figure 28 - Field Recorded GPS for Culvert Survey - Horizontal Gradient. A sustained deviation is present, indicated by the sharp, linear adjustments either side of the path error.

culvert is relatively noise free. A sustained path error is present during one line shown in Figure 28. Due to the duration of this error, the Kalman filter slowly accepts it as the best solution. This will be discussed further in *Discussion.*

4.3.1.2 Single GPS – Horizontal Gradient

The same satellite observations recorded by the Reach module were post processed to give a standard "single" mode receiver track. This is shown in red in Figure 30 (top, next page). Overlain in blue is the Kalman filtered track, using the position data and mean velocities obtained from the single mode positions. Figure 30 (bottom) shows the Kalman filtered single GPS (now orange) again, this time overlain with the post-processed differential track in black, which used the same observations but using differential corrections. Despite the error at line corners and the wandering Eastern record, the filtered result is very similar to the differential track. Use of the Kalman filter's control input matrix would alleviate the corner effects.

Magnetic data associated with the single mode GPS positions are likely to be poorly located and not representative of their actual sampled locations. In a local scale survey, the lack of accuracy and precision will mask any fine magnetic detail.

4.3.2 Vertical Gradient

The vertical gradient array survey was identical to the horizontal array survey, but with the system oriented vertically. This survey had a very poor GPS mount position, which is seen in the recorded position logs as very noisy location trails.

4.3.2.1 Field Recorded GPS – Vertical Gradient

Due to the poor antenna mount, there are several large and continual errors in the vertical array field recorded data. Errors with a smaller duration are easily minimised (Figure 29), however when the trail is lost for extended periods, especially at corners, it cannot maintain an accurate reconstruction of the path.

4.3.2.2 Single GPS – Vertical Gradient

The single mode GPS log has extensive errors, as a result of ground reflections and poor sky view. This survey was a worst-case scenario for the GPS. The Kalman filter performs well, reconstructing a discernible path (Figure 31, orange), however it does not recreate a comparable track to the
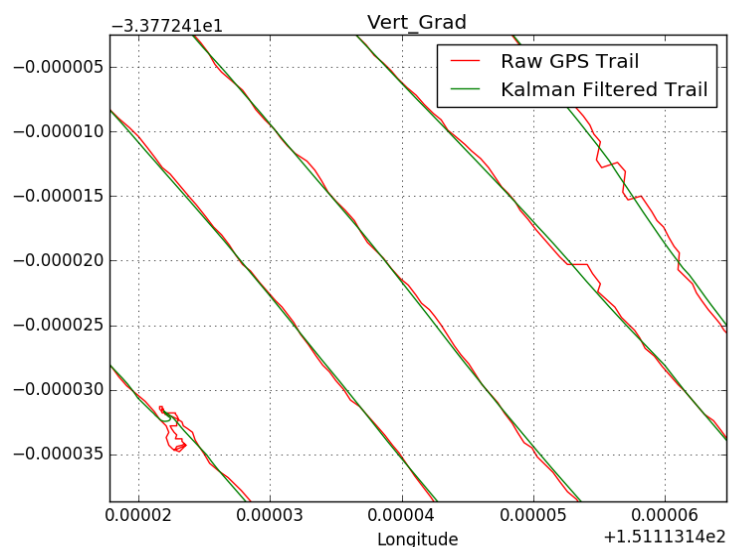

Figure 29 - Field Recorded Vertical Gradient Culvert Survey. Short deviations in the Single mode track are removed by the Kalman filter.

diffe
renti
al
(Fig
ure
31,
bott
om),
and
ther
e is
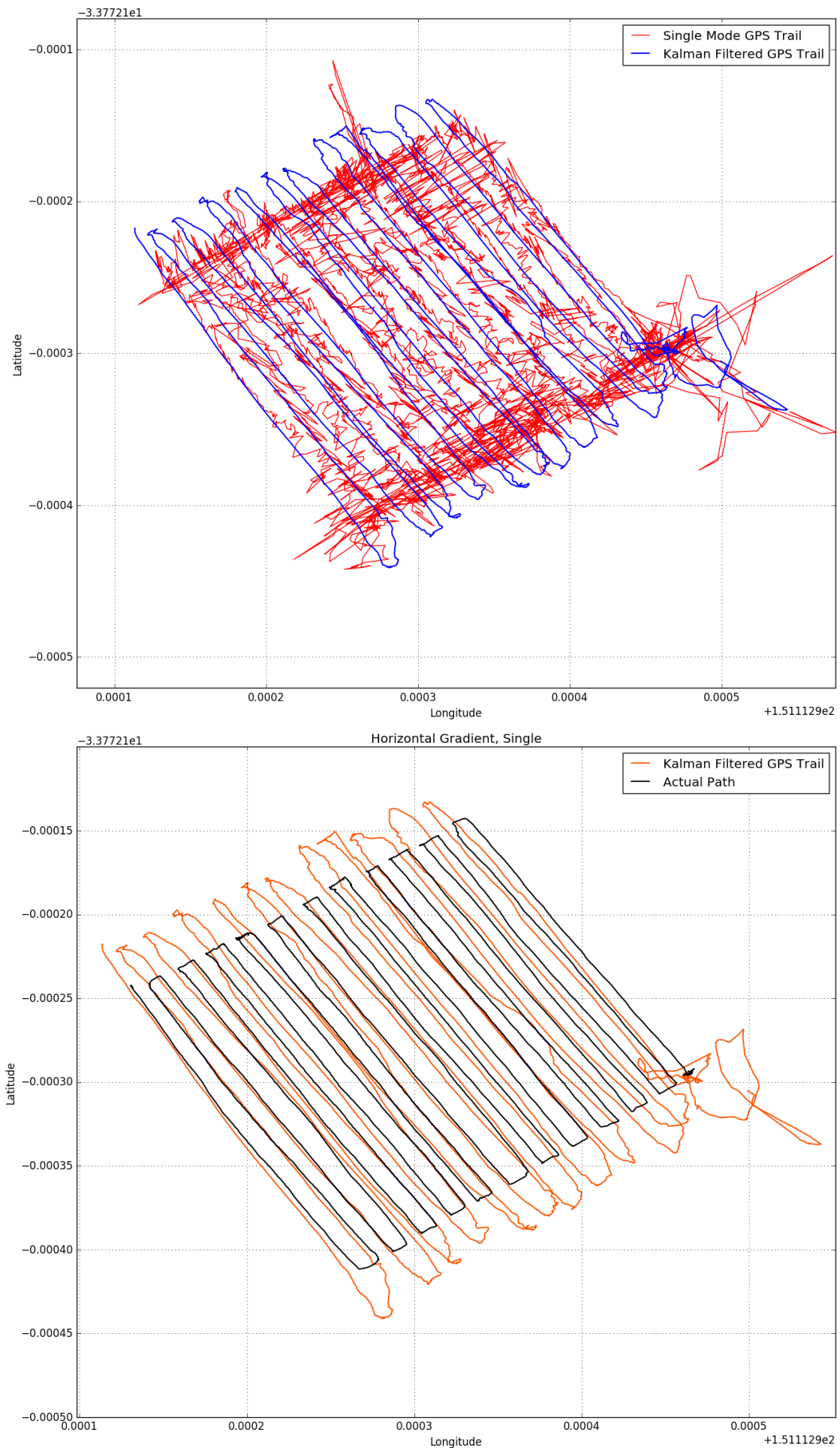signi
fican
t
over
lap
bet
wee
n
lines
.

Figure 30 - Horizontal Gradient Survey. Single (red) mode GPS trail compared to Kalman filtered Single mode (Orange) and post processed DGPS (Black)
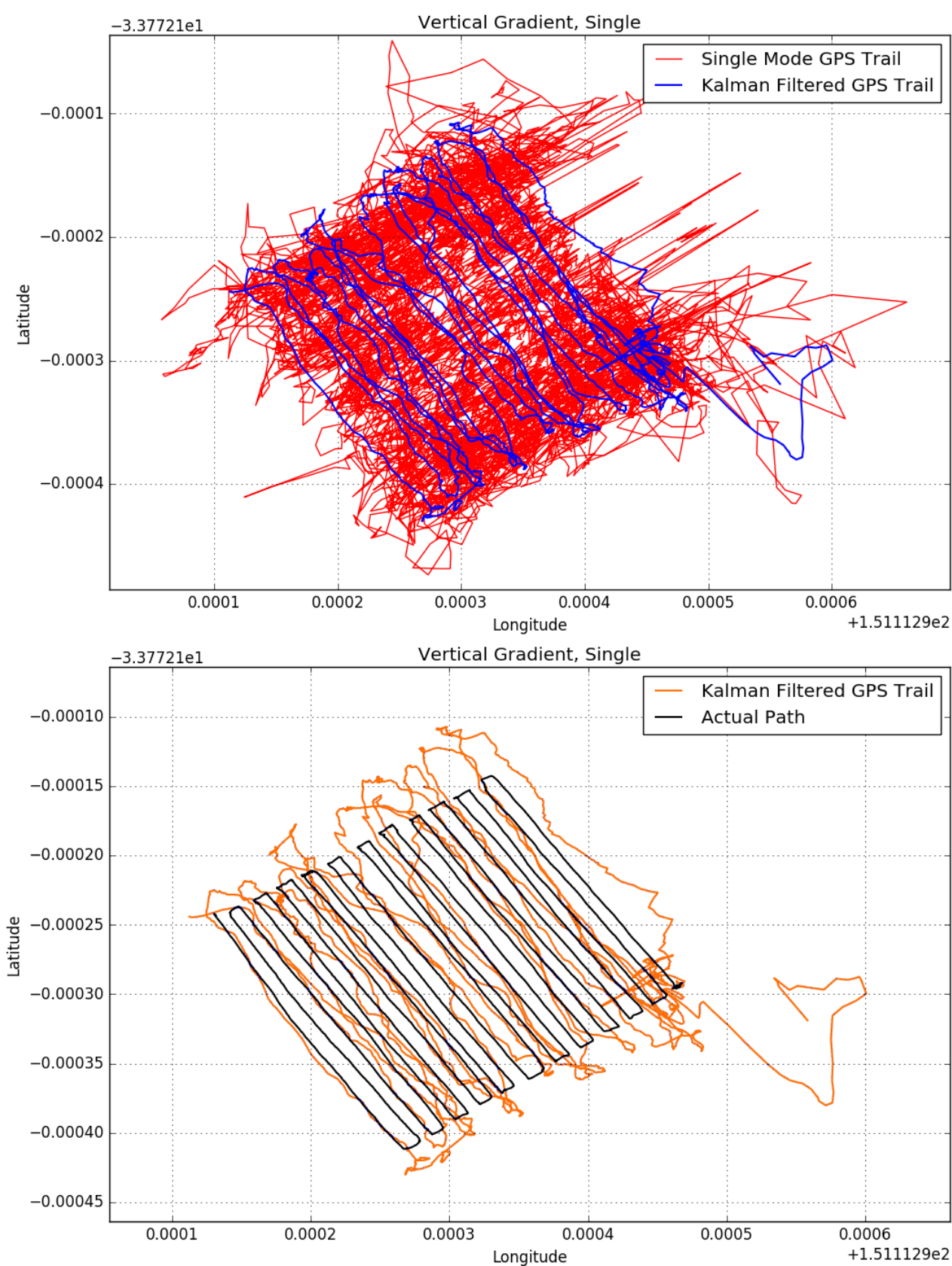
Figure 31 – Vertical Gradient Survey. Single (red) mode trail compared to Kalman Filtered Single mode (Orange) and post processed DGPS (Black). Considerable reconstruction is apparent through the use of the Kalman filter.

4.4 Sports Field Tests

Two tests were performed at the sports field, each with a North and South sub survey. These were defined by the halfway line of the field, as seen in the walked tracks of Figure 32. Performance of the aerial system was investigated, and trialled against the walked system. The walked full system surveys will provide a reference for the gradiometer magnetic response, while the higher speed drone survey will test the Kalman filter in lower sample density environments. The Southern field was flown first, followed by both walked surveys, then the Northern flight. A review of the Southern data revealed excessive magnetic noise that were not present during previous testing, as such all following lines were oriented East-West, which were known to not contain excessive noise. Figure 33 shows the flight paths for both flown surveys.
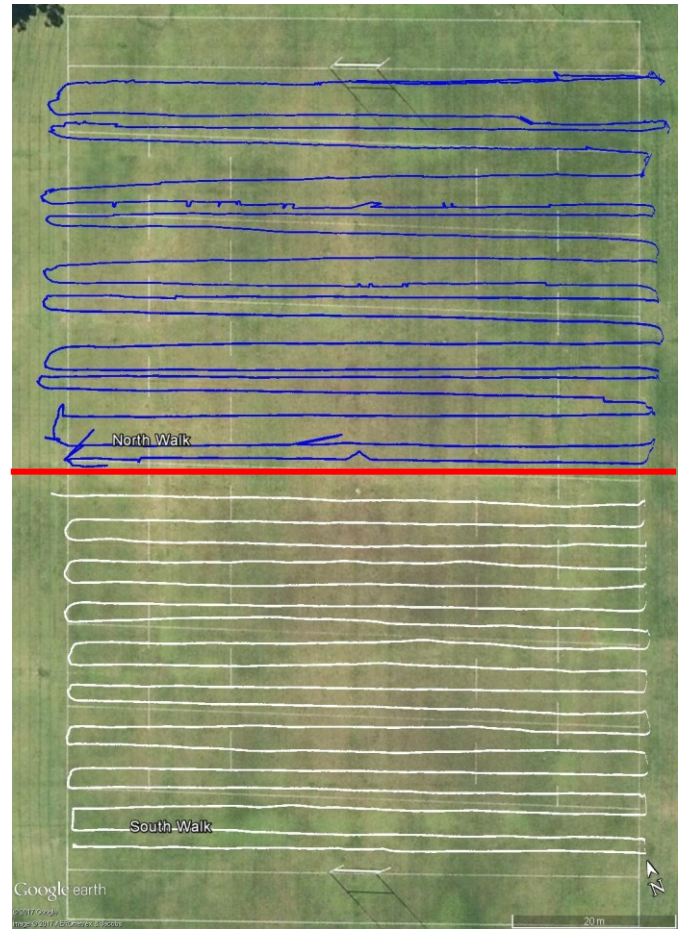

Figure 32 (Upper) - Field used for second test, with North (Blue) and South (White) sections indicated by their post-processed differential walked paths.

Figure 33 (Left) - Flight tracks using field based DGPS as recorded during flight. Green dots indicate Fix, Yellow Float, and Red Single mode positioning. Despite using a complete RTK differential GPS system, there are many deviations and DGPS drop outs during flights. This is hoped to be corrected with the Kalman filter

4.4.1 Walked Survey, North Field

4.4.1.1 Field Recorded GPS – North Walked

The walked grids show nearly perfectly accurate trails, with very little path deviation. In the North field walked grid, there are two small errors in the logged GPS track (Figure 34), which are easily accounted for by the Kalman filter. Due to the slow walking speed and good receiver location the differential data provide very accurate results. Magnetic data recorded at the positions logged here will be tightly grouped, and accurately positioned within the grid.
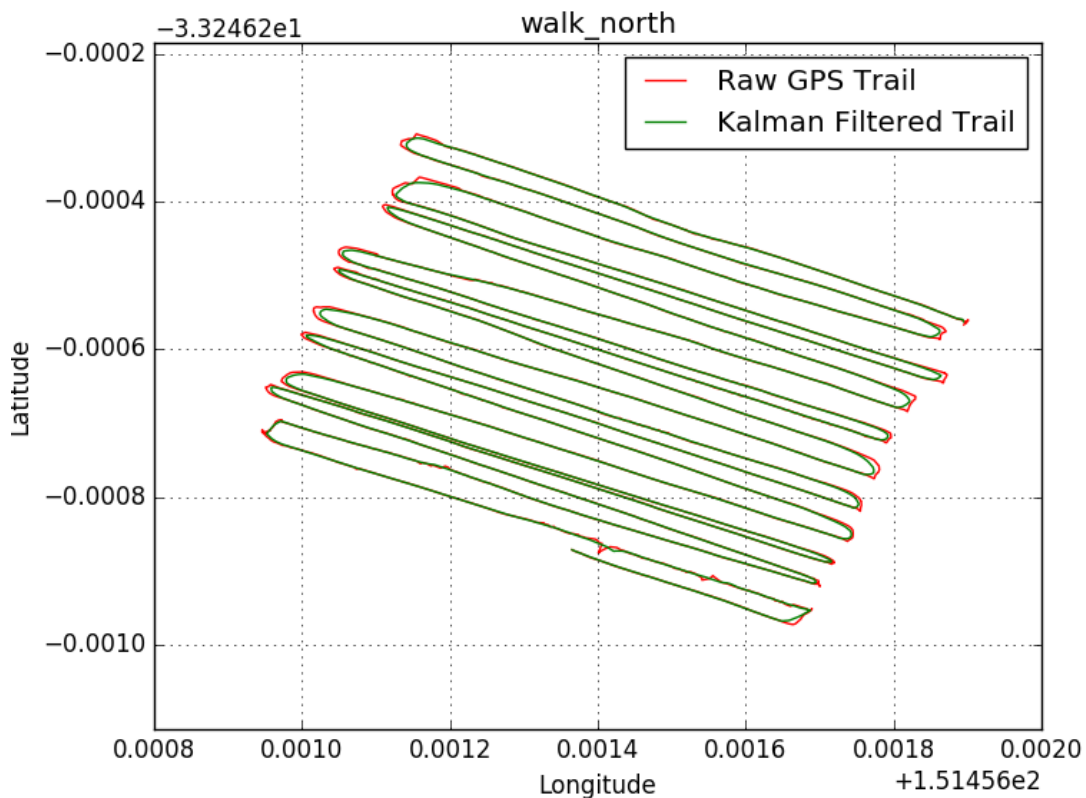

Figure 34 - North Field Walk Field Recorded DGPS Trail

4.4.1.2 Single GPS – North Walked

The North walk single GPS log has discernible survey lines in the single mode trail (Figure 35, top, red), however there is significant noise present. The Kalman filter successfully removes much of this noise. There is some path overlap between lines, shown in both the post processed differential (bottom, black) and Kalman filter output (orange). While the Kalman filtered track has much less noise, it is not very accurate to the recorded precise differential RTK track.
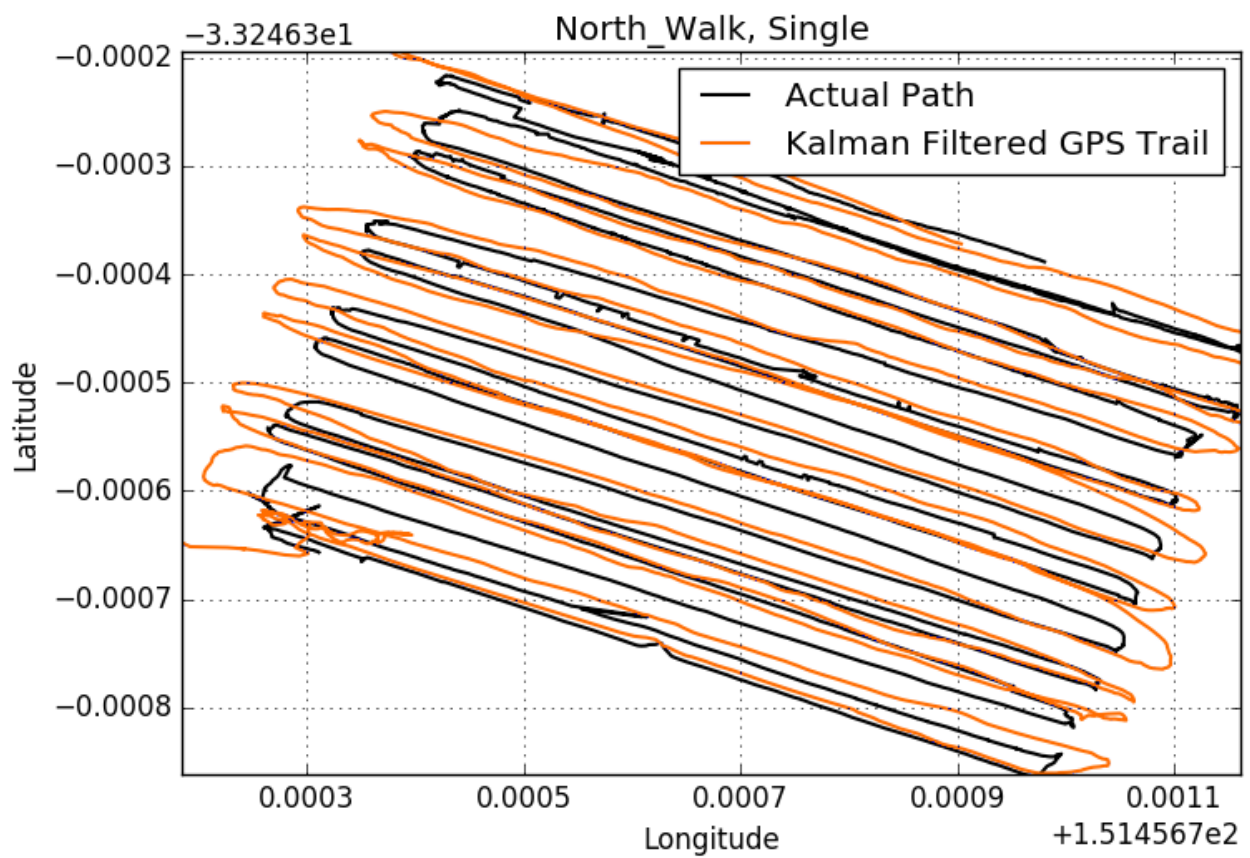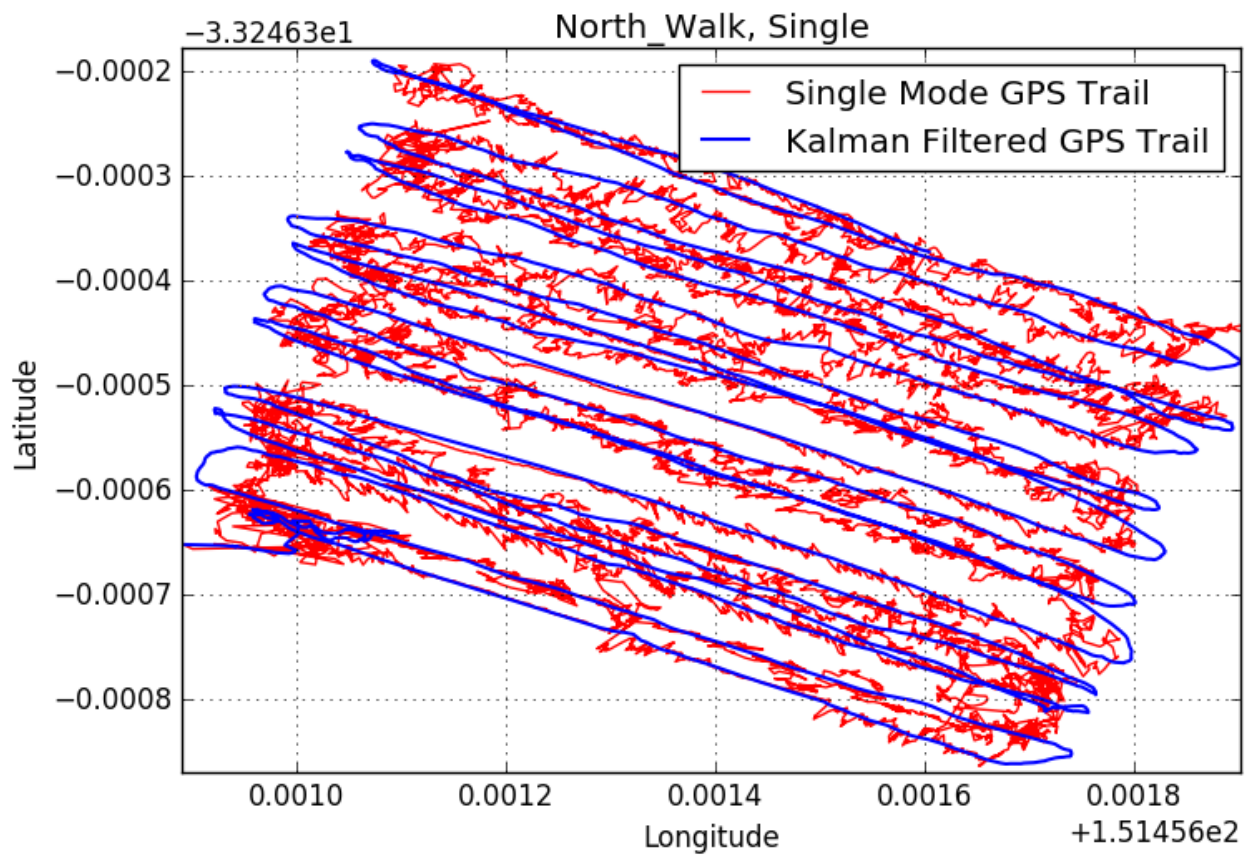
Figure 35 - North Walked Survey. Single (red) mode trail compared to Kalman Filtered Single mode (Orange) and post processed DGPS (Black)

4.4.2 Walked Survey, South Field

4.4.2.1 Field Recorded GPS – South Walked

The field recorded DGPS (Figure 36) trail is perfectly smooth already. No apparent errors are seen in the record. It is important to note the Kalman filter underestimates the shape of the corners. Supplying the Kalman filter with the control input matrix would alleviate these effects, as the control input supplies the filter with a more accurate initial prediction.
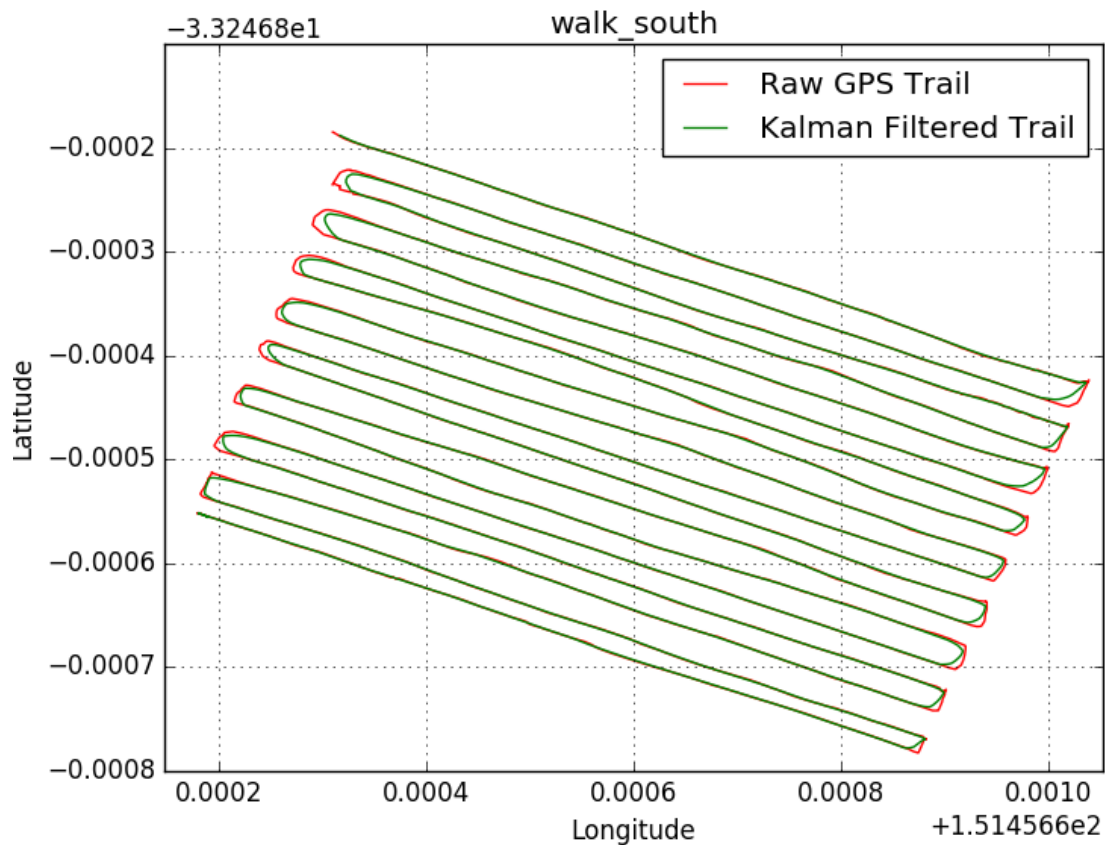

Figure 36- South Walked Survey Field Recorded DGPS track

4.4.2.2 Single GPS – South Walked

The single mode position log (Figure 37, top, red) for the walked southern survey has both low and high frequency positional noise. It is interesting to note smoothness of the field DGPS (bottom, black) despite the noise present in the single mode track. The longer frequency noise is predominantly in the N-S axis, and could not be smoothed by the Kalman filter, likely due to the extended duration of the errors.
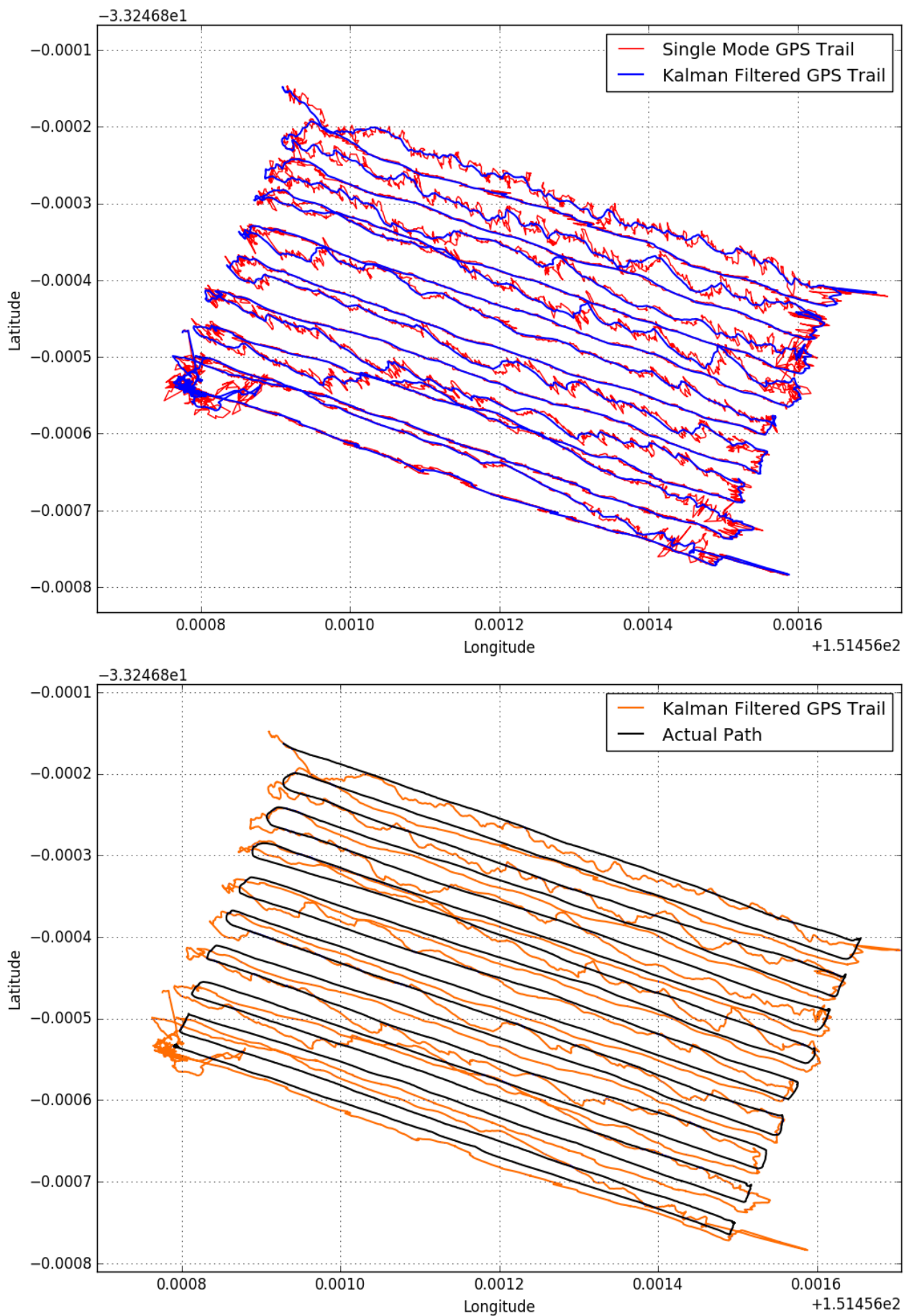
Figure 37 - South Walked Survey. Single (Red) mode trail compared to Kalman Filtered Single mode (Orange) and post processed DGPS (Black)

4.5 Flight Surveys

Flight surveys typically contain more path errors than their walked counterparts, likely due to the increased speed.

4.5.1 Flight Survey, North Field

4.5.1.1 Field Recorded GPS – North Flight

Despite the large path errors in the DGPS track shown in Figure 38, the Kalman filter manages to remove several large deviations present. The short duration of these errors means the Kalman filter maintains a high certainty for the duration of the error, however due to the velocity record introducing a slight lag, a small deviation is present after the initial two spikes.
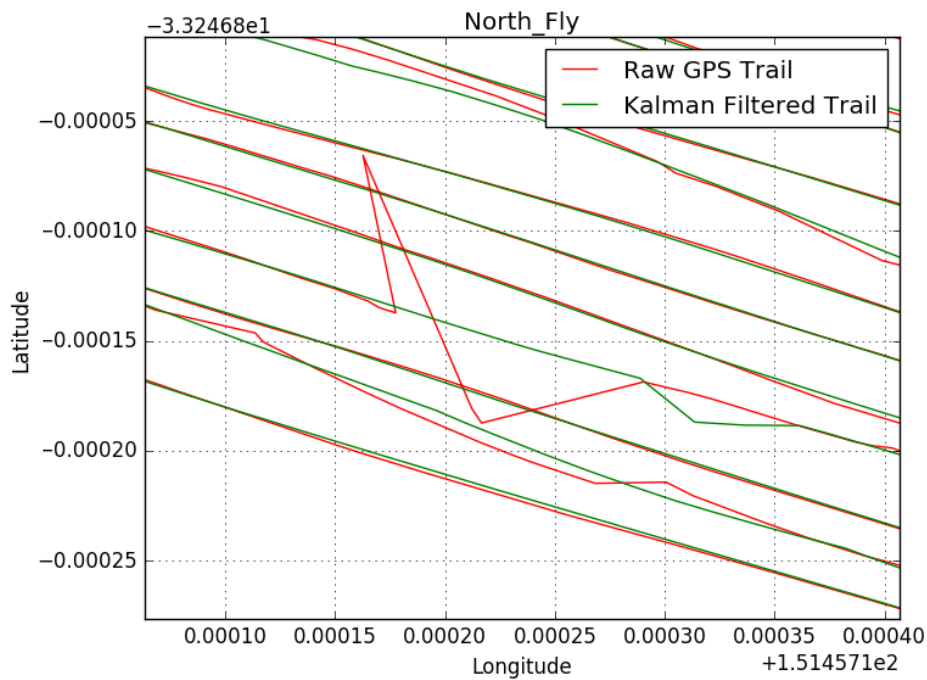

Figure 38 - Large deviations present in DGPS flight tracks are successfully removed.

4.5.1.2 Single GPS – North Flight

Similar to the above Single mode trails, the Northern flight (Figure 39) has abundant small deviations in the recorded single track (top, red), which are successfully removed with the filter (top, blue). A critically low battery caused autopilot to activate in the North-East corner, producing the erratic path. Comparison with the recorded Differential path (bottom, black) shows a generally good performance.
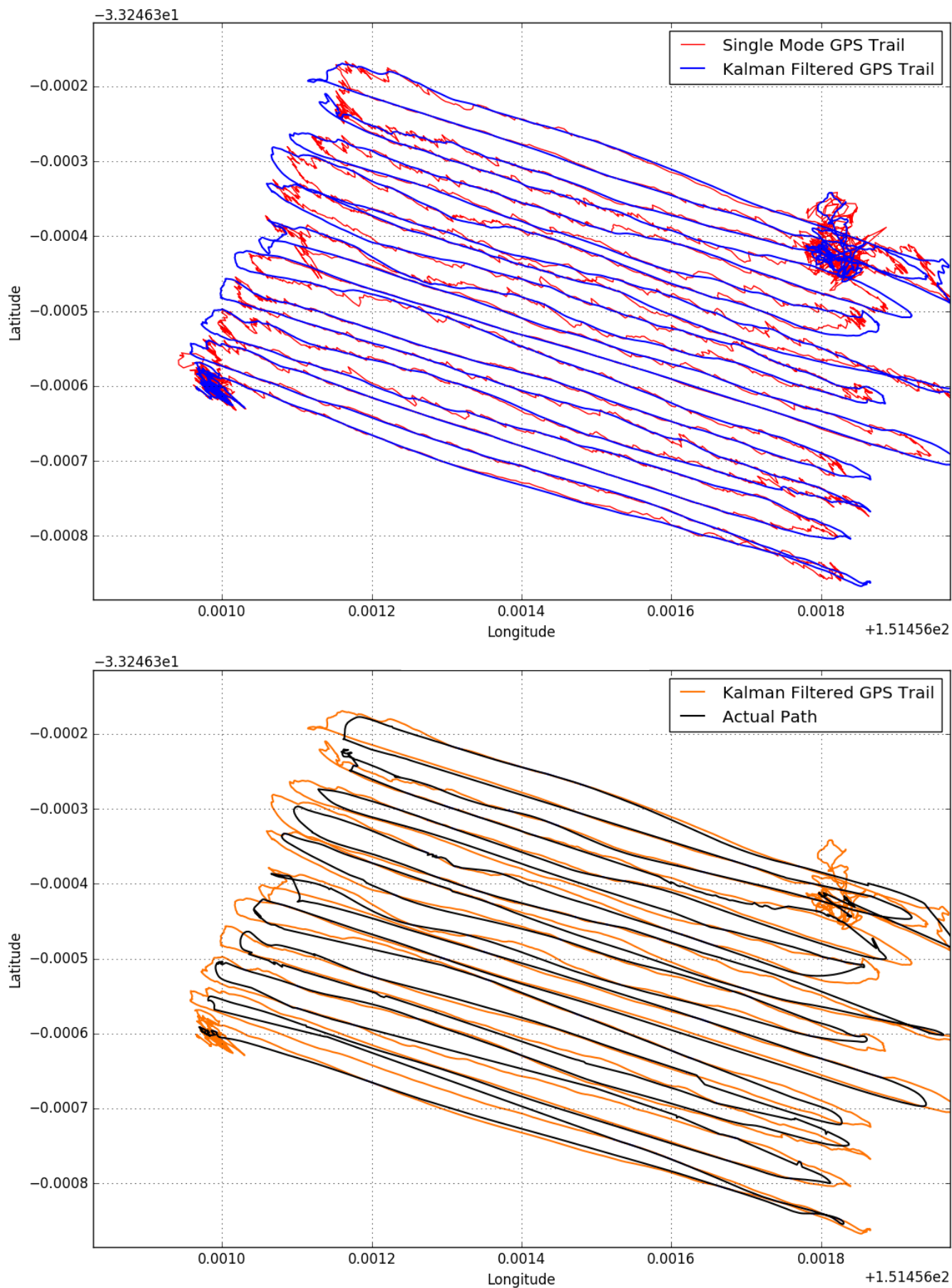
Figure 39 - North Flown Survey. Top: Single Mode GPS (Red) compared to the Kalman filtered single mode (Orang) GPS trail. Bottom: Kalman filtered Singe Mode GPS (Orange) compared to the post processed differential path (Black). Small path errors in single mode data are removed by the Kalman filter.

4.5.2 Flight Survey, South Field

4.5.2.1 Field Recorded GPS – South Flight

The Southern Flight was conducted in a North-South orientation. A large error is present in the field recorded DGPS trail (Figure 41, Red), where the Reach module held lost positioning for a short time. This was removed by the Kalman filter.
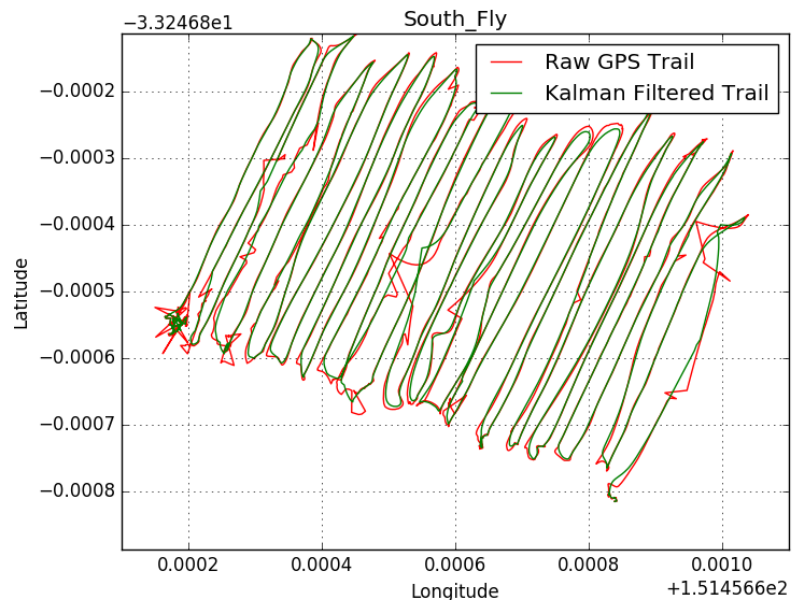

Figure 41 - South Field Flight Survey Field Recorded DGPS.

4.5.2.2 Single GPS – South Flight

The single mode trail of the Flight Survey (Figure 40, top, red) is remarkably precise already. Any small errors are smoothed effectively by the filter. The Kalman filtered solution and the field recorded differential tracks (bottom, black) are well correlated.
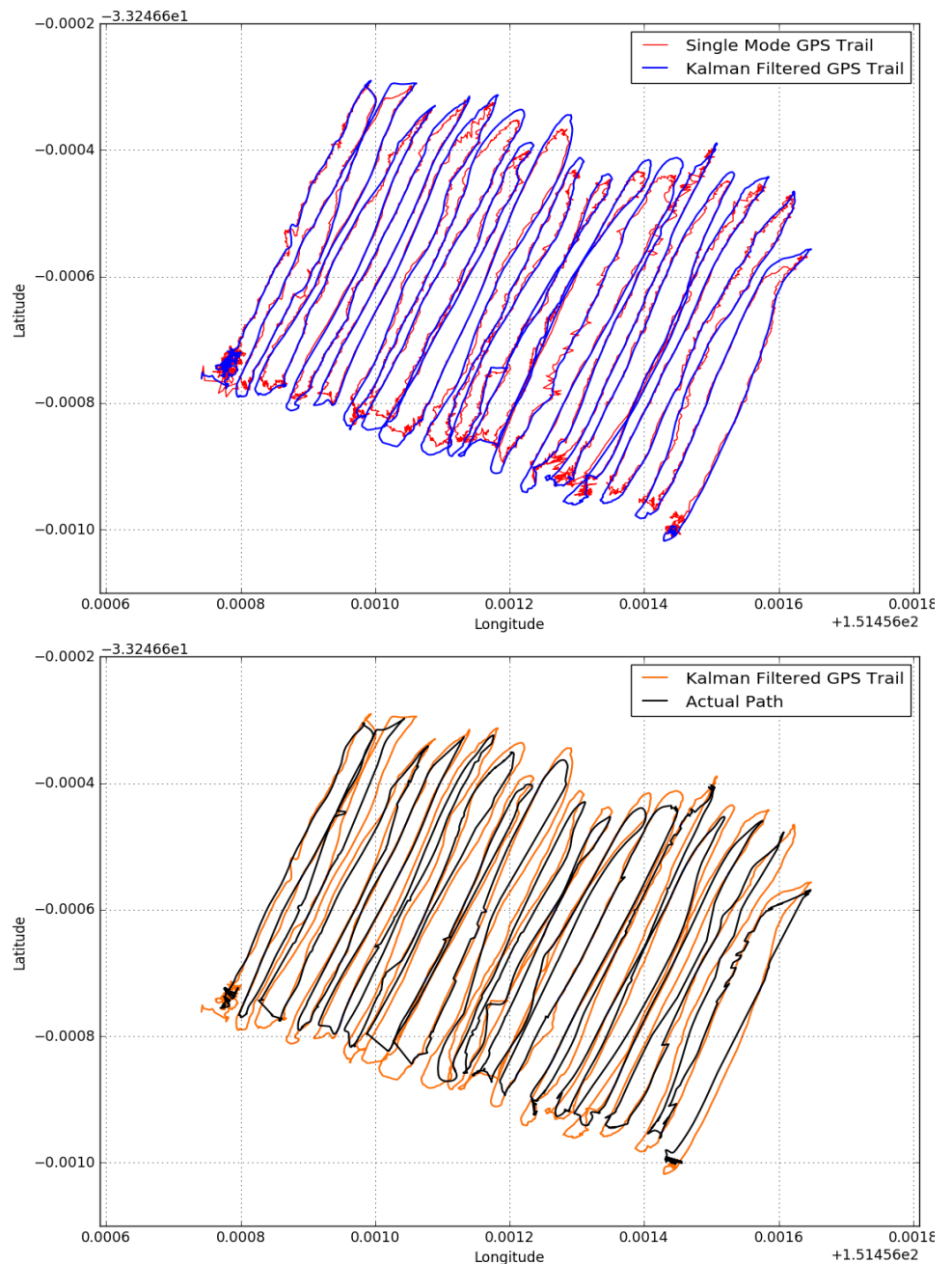

Figure 40 - South Field Flight Survey. Single (red) mode trail compared to Kalman Filtered Single mode (Orange) and post processed DGPS (Black)

4.6 Survey Magnetics

4.6.1 Proton Procession Magnetics

The Proton Procession magnetometer records total magnetic intensity (TMI), at discretely sampled points in a regular grid. TMI is not directly comparable to the vector or gradient readings from the gradiometer array, however comparisons can be drawn regarding the magnetic structure of the culvert. Figure 42 shows the TMI profile above the culvert. The culvert can be observed to enter the survey area to the central East, and exit in the Southern corner, and a metal drain is also present in the Western corner. The northern extent shows little response compared to the culvert.

Figure 42 - Proton Procession Extent and TMI above culvert. Red Dashed line indicates the interpreted culvert location, which can be compared to the indicated location in Figure 16.

4.6.2 Gradiometer Magnetics

4.6.2.1 Culvert Field Test - Gradiometer

The gradiometer system used on campus did not yet use an external 12-bit Analog to Digital Converter (ADC), which limited sensitivity to the 10-bit resolution of the Arduino, or approximately 250 nT per division. Figure 43 (Left) shows the horizontal array profile, while right shows the Vertical. The data are very noisy, and no correlation between the two profiles can be seen, likely due to the low resolution ADC used during the Culvert
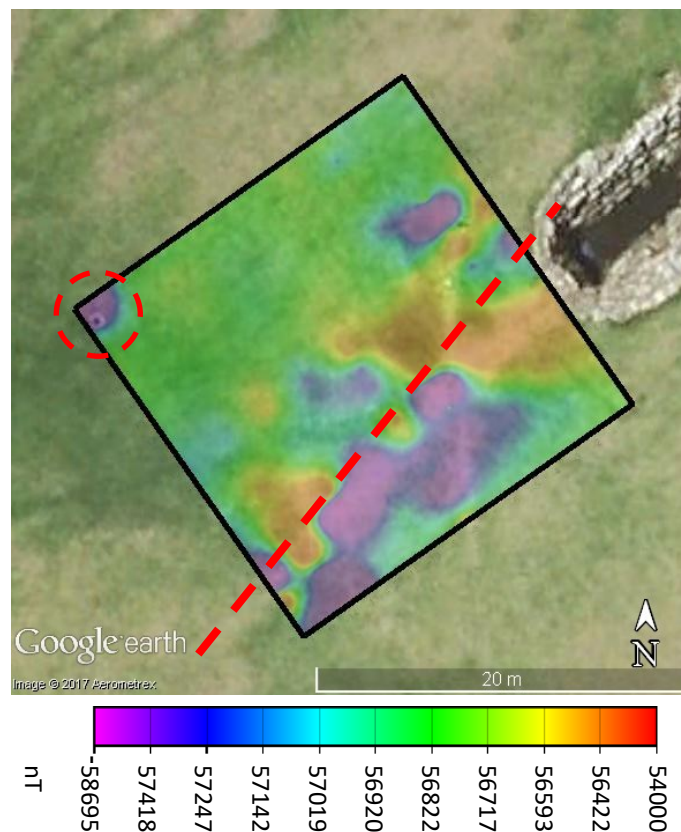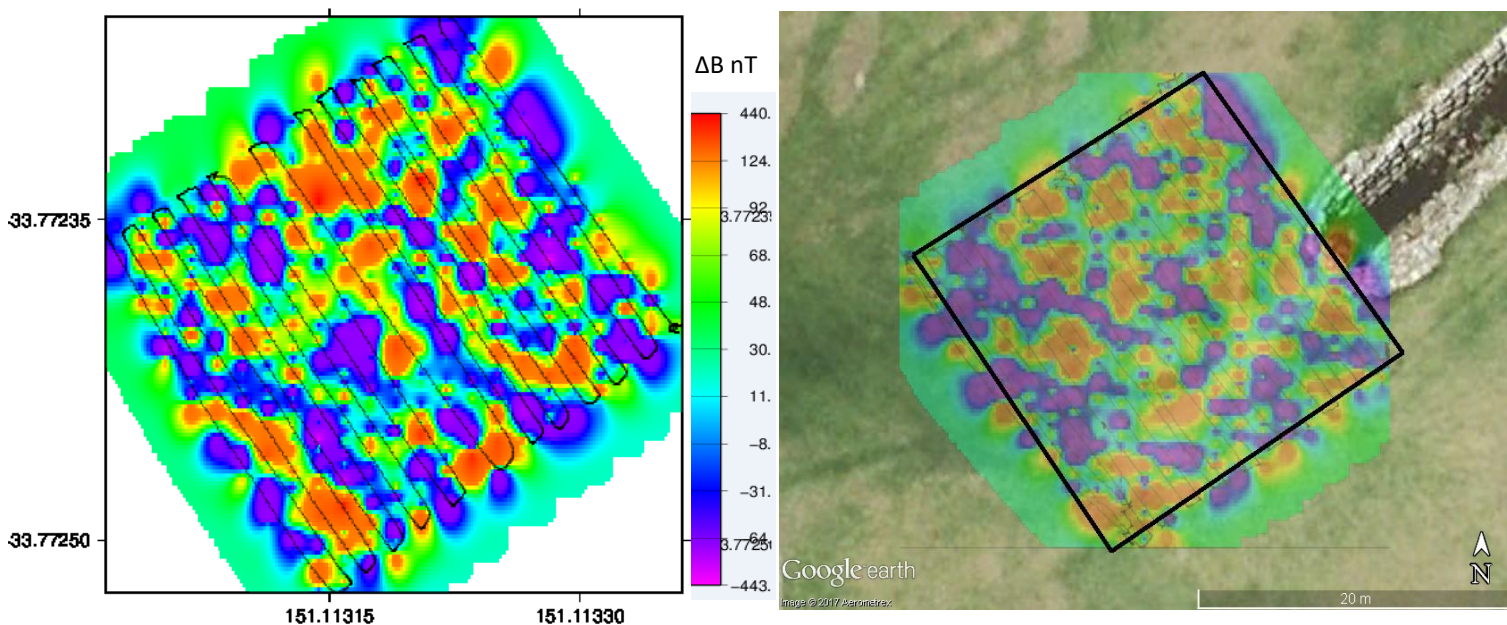

Figure 43 - Culvert Gradient Magnetic Profiles. Left, Horizontal Gradient and overlain DGPS path, Right Vertical Gradient over the Culvert. Only noise can be seen in these profiles.

survey, and the culverts depth.

4.6.3 Sports Field Test Magnetics

4.6.3.1 Walked Surveys – Magnetometer Sensitivity

Both North and South walked field tests had well positioned magnetic data. The array was attached to the UAV, which was carried while walking, and the system operated as normal in differential mode. Figure 44 shows the resulting magnetic gradient profile of the two surveys overlain in Google Earth.

The white line shows the field line locations, while black shows the walked path. Location of magnets and meteorite are shown (with the meteorite moved to be sampled again in the Northern section). As can be seen from the profile, the field is relatively magnetically quiet, other than the unusual low at the halfway line, and the response of the goal posts. In the Northern profile, both clusters of magnets can be seen clearly near their recorded locations, and there is a possible response from the
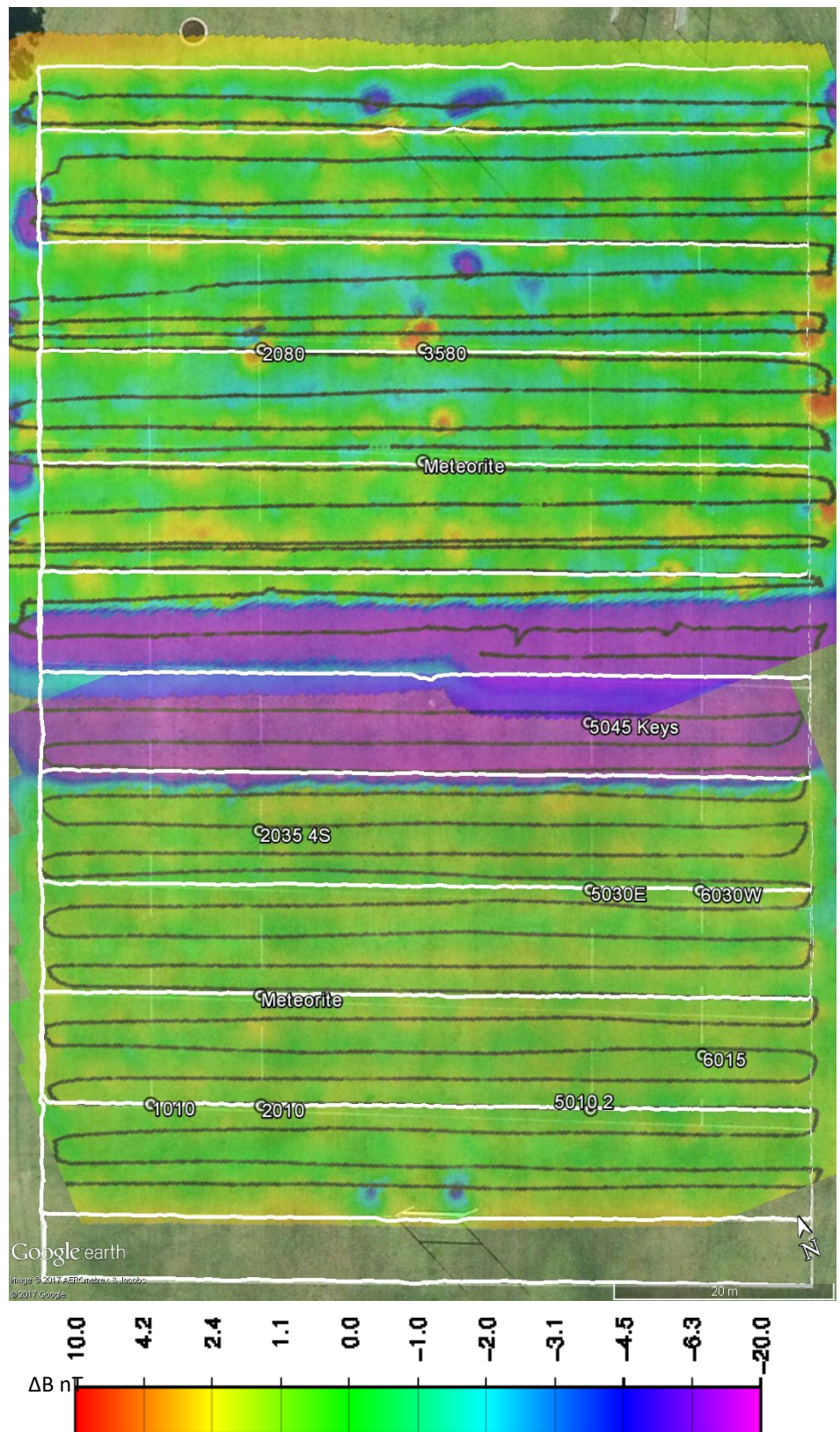

Figure 44 - Gradient magnetic response of magnetic targets on sports field. The white lines indicate surveyed field line markings, while black indicate the track of the North and South walked surveys, divided at the halfway line.

meteorite to the NNE of its recorded location. Positions of Northern targets were not GPS surveyed due to miscommunication, so the recorded positions are estimated according to their placement on marked field lines so some offset may be present. Corners in the North survey were taken with a simulated banking motion, which has given rise to the anomalies present at each line end. The central low is present in all surveys, in the record of the same magnetometer each survey, and occurs within each 10 m section adjacent to the centre line. It is unknown if this is a real signal, possibly arising from irrigation or electrical cables, or potentially some unknown error in hardware that occurred at the end of the Southern survey and persisted through flight surveys, only to be corrected a short way into the Northern Survey. No targets can be identified in the Southern survey, and the only visible response is from the goal posts. Unlike the Northern survey, only one cluster of 4 magnets was present which was not detected.

Due to high central response, a second grid was mapped with the anomalously large values removed from the end of each survey and the colour map refit. It is uncertain where the large responses originated, and is thought to be a hardware error. These are presented in Figure 45. With the lower range of flux densities, the colour palette is less compressed, and line levelling
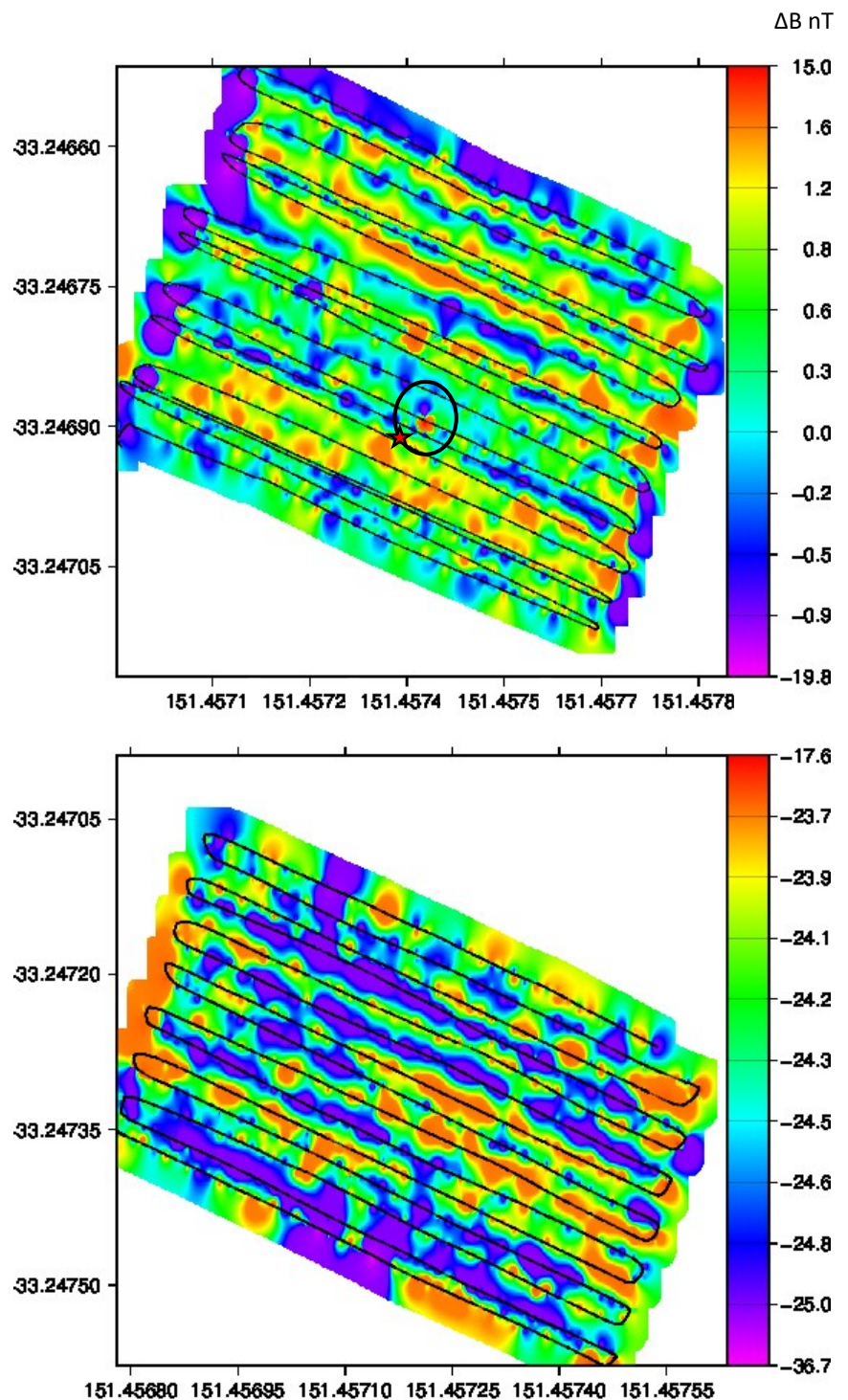

Figure 45 - Reduced range magnetic response of the walked surveys, North (top) and South (bottom) field surveys. Line level issues are apparent, even in the walked system. A strong dipole (top, circled) is located near the location of the meteorite (star). No targets are identifiable in the South. Position data are using differential GPS.

issues become apparent. No confident targets are presented in the South walk with the reduced range data. A strong magnetic dipole near the location of the meteorite is visible in the Northern data. The magnet clusters are reduced in visibility compared to Figure 44.

4.6.3.2 Walked Surveys – Kalman Filtered Magnetic Plots

Figure 46 shows the same magnetic profiles, but with single mode recorded sample positions. The black track marker shows the noisier position log in the single mode trail. A marked response is visible only in the Kalman filtered profile. While it is several metres from the meteorite location, it is greatly reduced in magnitude in the Single mode data. The possible causes of this are discussed in *Discussion.*
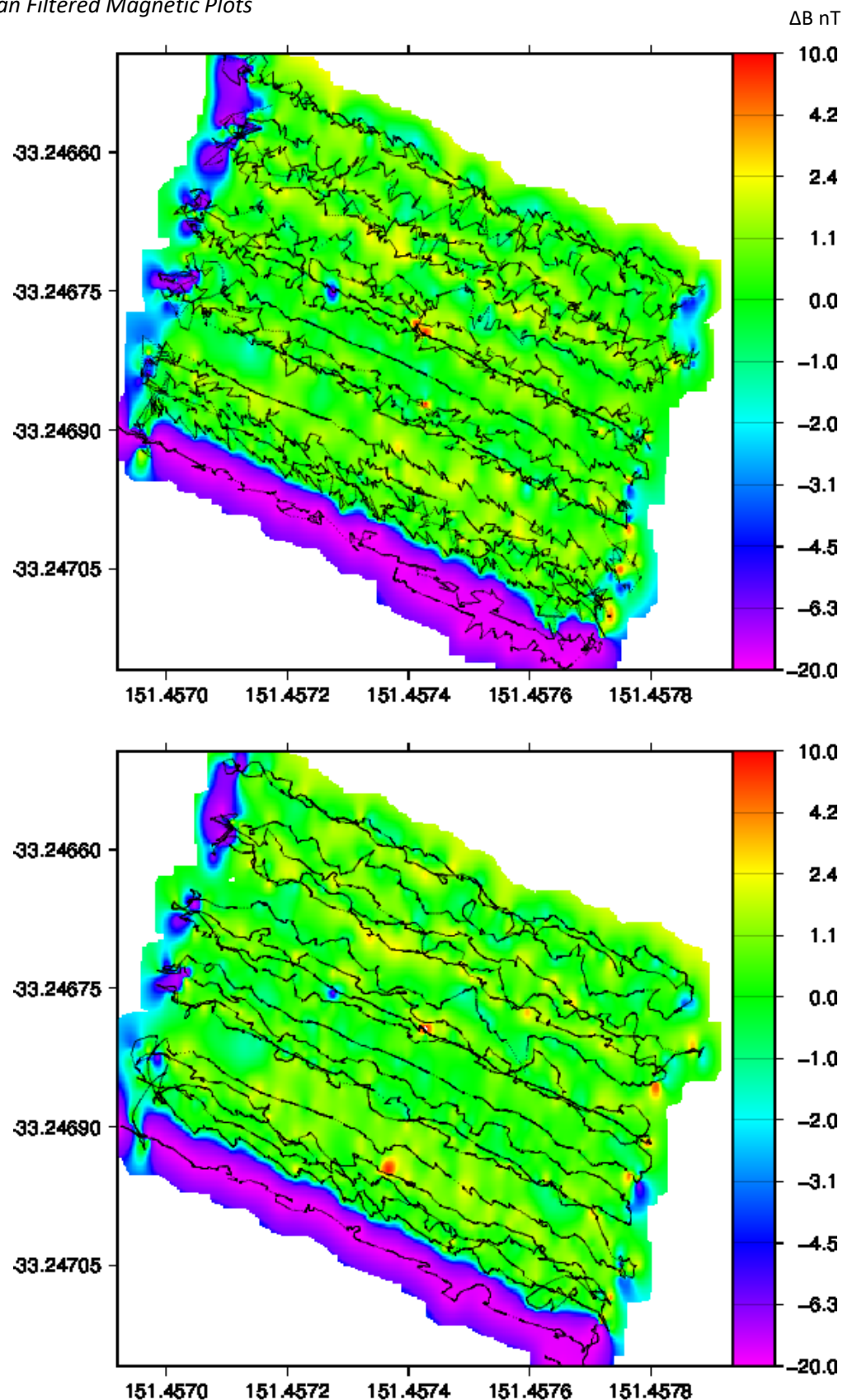

Figure 46
Above - Single mode, north walked magnetic profile.

Below - Kalman filtered positioned of same profile.

Units indicate the average differential between each sensor pair.

4.6.3.3 Flight Survey – North Field

Figure 47 shows the magnetic profile recorded by the DJI Phantom 3 carried magnetometer array. The magnet cluster labelled 2080 is shown as a dipole response, however the second cluster and meteorite are not resolved. Similar to the walked surveys, line levelling issues remain apparent, and the large low response is present in the 10m adjacent the centre line.
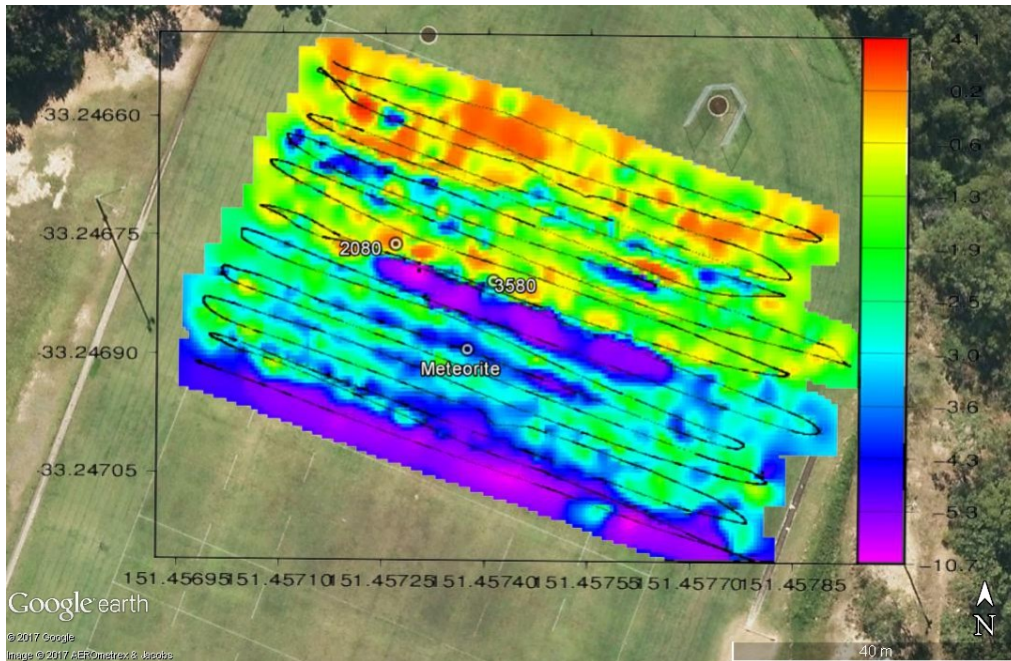
Figure 47 - North Field, Field Differential GPS Magnetic Profile. A Dipole response is seen at the labelled 2080 magnet cluster, but no response is seen for the 3580 cluster or meteorite. Line levelling remainsl an issue.

4.6.3.4 Flight Survey – South Field

The South field magnetics were the first survey of the day. Obvious line errors are present, and no magnetic targets are seen. This prompted the change to E-W survey lines for later surveys.

Figure 48 – South Field Magnetics – Lines flown North South present very poor line level effects. No satisfactory grid could be generated using these data collected N-S.

4-52

Chapter 5 - Discussion

In addition to a review of the filter and UAV performance findings here, there are several aspects to this research that merit further discussion. They fall broadly into the subjects of System Design, Processing, and the current state of UAV geophysics.

5.1 System Performance

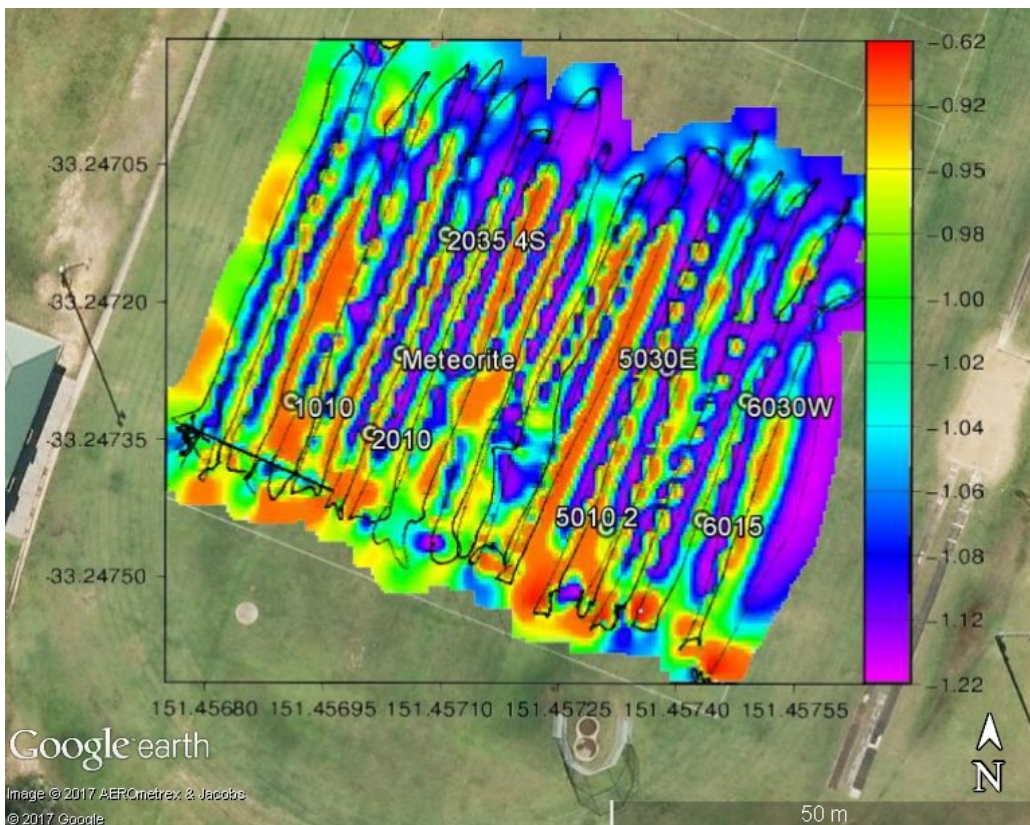Real Time Kinematic GNSS offers exceptional precision and accuracy in both ground and aerial surveys, when good sky view, multiple constellations and a base station correction provider is available. Some path errors are introduced when fewer satellites are available or the base station link drops out. The Kalman filter implementation presented here has been shown to recover more accurate ground tracks during these times. Furthermore, the Kalman filter dramatically enhances single mode GNSS tracks, as seen in Figure 30 and Figure 31.

The performance of the filter used in this research likely depends greatly on the regular grid lines flown. With only satellite determined position and velocity products from those, the system remains entirely reliant on the GNSS receiver performance and a smooth ground track. Addition of external sensors, such as a 3D compass, airspeed indicator or accelerometers/gyrometers could provide the filter with additional constraints that do not rely on previous positions, potentially alleviating the cornering effects. These sensors could also further refine magnetic data acquired, such as tilt correction and vertical continuation for levelling.

The quality of the magnetic measurements was mostly poor. Data acquired above the culvert, prior the use of a higher resolution ADC, could not show the culvert extent conclusively. In the walked sports field tests with field recorded DGPS, the two magnet clusters were well located, while the meteorite was possibly shown several metres distant from its marked position. Despite the clear responses in the North, no individual magnets, or the meteorite could be seen in the South profile. This may be due to the orientation of the meteorite providing a weaker dipole response to the array, or simply line noise being greater for that line. Use of the UXO detection method described by Munschy et al., (2007) for along line UXO may be a possible method to resolve this problem.

Flight magnetics show similar variability, with more noise. Only a single magnet cluster was resolved by the gradient array, and lines retained levelling issues. Aerial surveys provided a much faster acquisition than walking, in these surveys by approximately 3 times. A single battery provided flights between 10 to 15 minutes duration, depending on speed and wind conditions, while walked surveys took up to 35 minutes. Flight speeds may be able to increase in future tests, if the magnetic sample rate can be increased to maintain sample density.

Overall, performance of the magnetic system was limited by the UAV and magnetometer hardware. Development of a custom UAV to measure and limit motion noise, as well as further separate magnetometers and motors, began too late to investigate the potential performance increases offered by UAV design.

5.2 Further System Design

Beyond performance of the system, there are several key additions that could greatly enhance the capability of the system. First, the addition of a stabilising gimbal would limit orientation changes and flight motion of the gradiometer, further reducing motion noise. Second, more sensitive magnetometers, such as the Stefan Mayer FL1-100 would enhance magnetic detection. These require a bipolar 12 V power supply, which was not readily implementable during this thesis. Third, it is possible to stream the Arduino measured data over radio link, just as GNSS corrections are broadcast from the base station. It is possible to view and filter these data in real time on PC or mobile ground station, and flight path could be adjusted accordingly. This particular goal of real time data monitoring was noted by Malehmir et al., (2017), and while not implemented during surveys, was achieved during testing of the systems presented here.

Many of these goals would be aided by the construction of a custom UAV, such as the one under initial work presented here. While the system was capable of flying the array autonomously, motor and flight controller tuning had not been carried out to attain satisfactorily stable flight. It is predicted the larger capacity battery and energy efficient motors would allow longer flight times, the custom frame superior mounting, and the native GPS integration superior DGPS stability. Open source and accessible flight data available with Ardupilot could be integrated with the Kalman filter, or processing of data such as line levelling, and noise qualification.

It is apparent some levelling is required between alternate lines in the walked surveys, and between points in the aerial surveys. The RTK GPS system provides a highly accurate vertical position in addition to its lateral measurements, and so a vertical continuation could be performed

with reasonable accuracy to alleviate these effects. The Kalman filter could also be easily updated to also process vertical errors as another state. With additional sensors, such as an altimeter or laser range finder, the vertical position can be refined further. An additional continuation may be required for each sensor in the array, as tilt about the axis perpendicular to the array will raise or lower each sensor, relative to their distance from the centre of gravity. Logging of array tilt with a simple accelerometer, combined with this distance, could be used to level each sensor.

Tilt can also affect the sampled magnetic field in a vector magnetometer such as the fluxgate magnetometer. A change in the orientation of the sensing axis will change the component of the magnetic field. In a gradient system where the sensing axes are aligned, these effects are removed.

Additional equipment could be used on a UAV to detect meteorites. Of note of course are cameras, however as mentioned in the introduction, there are times meteorites will be undetectable due to surface cover. The use of an infrared camera, to image the heat difference between iron meteorites and background due to their thermal conductivity difference at dusk has been suggested but remains to be investigated.

In the field of magnetic gradiometry, there are two considerations for this system. The first is array length, which on the very small UAV here was 1m. Increasing array length increases the gradient response, however larger arrays become unwieldly on small UAVs. A potential solution to this is the use of in-line gradiometry, using a single, fixed orientation sensor at different positions. With the enhanced positional accuracy of the Kalman filtered tracks this could be a viable addition to the system.

5.3 Kalman Filter Tuning

The performance of the Kalman filter is reliant on the input measurement and process error matrices. Each matrix adjusts the calculated weighting of the data used for state estimation, and by altering these terms the output combination of measurements and prediction are changed. In the presented results, an optimal choice of the process error and measurement error were selected by eye. This method was inefficient as optimal values are unique for each acquisition mode. Statistical investigation to determine optimal parameters can be performed (eg, Gomez-Gil et al., 2013) to obtain repeatable and mathematically reasonable error matrices.

With the selected parameters and system model, the presented filter repeatedly overshot the end of each line. This is due to the model relying on past velocities and the system error (P) changing slowly as a result of the chosen parameters, which were selected to smooth along line deviations most effectively. Reducing the overshoot by changing the input error matrices would reduce the performance of along line deviation removal.

Regarding the Kalman filter, it is possible to run a "backwards" pass after all data has been collected, using the RTS smoother as described in Section 3. This would then integrate the forward and backward filter results, weighted according to the recorded state error covariance matrix at each point, resulting in an output path with no directional lag which could be seen in Figure 28.

Chapter 6 - Conclusions

This thesis aimed to implement precision positioning techniques on a very small UAV for application in geophysical exploration, with a specific focus on meteorite search and retrieval. This was realised through the use of a miniature, real time kinematic, differential GPS receiver and a Kalman filter implementation. Common GPS path errors arising from satellite drop-outs, base station availability and interference were smoothed by the filter implementation, and the effect of this smoothing on magnetic gradient profiles was demonstrated.

Magnetic gradient data were shown for the purpose of demonstrating positional logs with associated geophysical data across the operation of different GPS accuracy status'. This also fulfils the secondary aim of this thesis, in the construction of a geophysical UAV utilising precision GPS.

A gradient magnetometer array was constructed and integrated with a very small UAV for testing of the position data. This system performed well, and was successful in locating targets in both walked and aerial surveys, however with variable reliability. The sensitivity of the magnetometers is believed to be the limiting factor. This, and other aspects of the system could be improved or built upon with further work.

Numerous follow on research aims were identified, primarily the levelling of lines through vertical continuation, the addition of secondary sensors for Kalman filter performance, and UAV platform redesign. At the current system weight, there are several hundred grams to utilise before reaching the 2 kg unrestricted licence class maximum. The first addition would be real time data monitoring and processing via radio link, which was tested during this thesis but not implemented. With the logfile streaming to a ground station in real time, data could be filtered and plotted on the fly, and measurement quality observed during flight. The second hardware addition would be an array gimbal, to limit motion noise during flights. A gimbal was designed and built as a concurrent bachelor of mechanical engineering thesis for the array presented here, but was unavailable for field trials.

The enhanced accuracy arising from the application of the Kalman filter to RTK DGPS tracks can be used to more tightly constrain geophysical sample locations on rapidly moving sensors, such as UAVs. It is hoped these findings, and the development of a very small UAV magnetic gradiometer, can be applied to future systems in the search for meteorites.

Chapter 7 - References

Ardupilot, 2016. Ardupilot. *Available online:* http://ardupilot.org/

Bland, P.A., Towner, M.C., Sansom, E.K., Devillepoix, H., Howie, R.M., Paxman, J.P., Cupak, M., Benedix, G.K., Cox, M.A., Jansen-Sturgeon, T. and Stuart, D., 2016. Fall and recovery of the Murrili meteorite, and an update on the desert fireball network. *LPI Contributions*, *1921*.

CASA, 2017. AC 101-10 Remotely piloted aircraft systems – operation of excluded RPA (other than model aircraft).

Doll, W.E., Gamey, T.J., Beard, L.P. and Bell, D.T., 2006. Airborne vertical magnetic gradient for near-surface applications. *The Leading Edge*, *25*(1), pp.50-53.

Dow, J.M., Neilan, R.E. and Rizos, C., 2009. *The international GNSS service in a changing landscape of global navigation satellite systems*. Journal of Geodesy, 83(3), pp.191-198.

Emlid, 2017. Reach RTK docs. *Available online: https://docs.emlid.com/reach/*

Eueler, H.J. and Goad, C.C., 1991,. *On optimal filtering of GPS dual frequency observations without using orbit information.* Bulletin Geodesique, 65(2), pp.130-143.

Eriksson, S., Real-time kinematic positioning of UAS-possibilities and restrictions. MS thesis, online: http://publications.lib.chalmers.se/records/fulltext/246159/246159.pdf

Faragher, R., 2012. Understanding the basis of the Kalman filter via a simple and intuitive derivation [lecture notes]. *IEEE Signal processing magazine*, *29*(5), pp.128-132.

Fireballs in the Sky, 2016. Kati Thanda Impact Feature. *Available online:* http://fireballsinthesky.com.au/2016/01/digging-up-the-dfns-first-meteorite/

Gavazzi, B., Le Maire, P., Munschy, M. and Dechamp, A., 2016. Fluxgate vector magnetometers: A multisensor device for ground, UAV, and airborne magnetic surveys. *The Leading Edge*.

Geoscience Australia, 2017. AUSCORS, *Available online:* https://www.auscors.ga.gov.au/

Gomez-Gil, J. et al., 2013. A Kalman filter implementation for precision improvement in Low-Cost GPS positioning of tractors. Sensors (Switzerland), 13(11), pp.15307–15323.

GPS Directorate, 2016. Systems Engineering & Integration Interface Specification, NAVSTAR GPS Space Segment/Navigation User Segment Interfaces, IS-GPS-200.

GPS.gov, 2017. New Civil Signals. *Available online: http://www.gps.gov/systems/gps/modernization/civilsignals/*

Grewal, M.S. & Andrews, A.P., 2001. Kalman filtering: theory and practice using MATLAB

Grewal, M.S., 2011. Kalman filtering. In *International Encyclopedia of Statistical Science* (pp. 705-708). Springer Berlin Heidelberg.

Groves, P.D., 2013. Principles of GNSS, inertial, and multisensor integrated navigation systems. Artech house.

Howie, R.M., Paxman, J., Bland, P.A., Towner, M.C., Cupak, M., Sansom, E.K. and Devillepoix, H.A., 2017. How to build a continental scale fireball camera network. *Experimental Astronomy*

Hofmann-Wellenhof, B., Lichtenegger, H. and Wasle, E., 2007. *GNSS–global navigation satellite systems: GPS, GLONASS, Galileo, and more*. Springer Science & Business Media.

ICSM, 2016. Surveying for Mapping. Intergovernmental Committee on Surveying and Mapping. *Available online:* http://www.icsm.gov.au/mapping/surveying4.html

IGS, 2017a. IGS Products. *Available online:* http://www.igs.org/products/data

IGS, 2017b. SYDN7 Site. *Available online:* http://www.igs.org/igsnetwork/network_by_site.php?site=sydn

Kalman, R.E., 1960. *A New Approach to Linear Filtering and Prediction Problems.* Journal of Basic Engineering, 82(1), p.35.

Macke, R.J., 2010. Survey Of Meteorite Physical Properties Density, Porosity And Magnetic Susceptibility.

Malehmir, A., Dynesius, L., Paulusson, K., Paulusson, A., Johansson, H., Bastani, M., Wedmark, M. and Marsden, P., 2017. The potential of rotary-wing UAV-based magnetic surveys for mineral exploration: A case study from central Sweden. *The Leading Edge*, *36*(7), pp.552-557.

Microchip Technology Inc, 2017. MCP3424. *Available online:* http://www.microchip.com/wwwproducts/en/MCP3424

Munschy, M., Boulanger, D., Ulrich, P. and Bouiflane, M., 2007. Magnetic mapping for the detection and characterization of UXO: Use of multi-sensor fluxgate 3-axis magnetometers and methods of interpretation. *Journal of Applied Geophysics*, *61*(3), pp.168-183.

National Instruments, 2016. GPS Wireless Standard. National Instruments. *Available online*: http://www.ni.com/tutorial/7139/en/

Paxman, J.P., Bland, P.A., Howie, R.M., Towner, M.C., Cupák, M., Devillepoix, H.A. and Sansom, E.K., 2016, November. The desert fireball network: A sensor network for meteorite tracking and recovery. In Control, Automation, Robotics and Vision (ICARCV), 2016 14th International Conference on (pp. 1-6). IEEE.

Ranacher, P. et al., 2016. *Why GPS makes distances bigger than they are*. International Journal of Geographical Information Science, 30(2), pp.316–333.

Rauch, H.E., Tung, F. & Striebel, C.T., 1965. *Maximum likelihood estimates of linear dynamic systems*. AIAA Journal, 3(8), pp.1445–1450.

Schmidt, P.W. and Clark, D.A., 2006. The magnetic gradient tensor: Its properties and uses in source characterization. *The Leading Edge*, *25*(1), pp.75-78.

Smith, D.L., Ernst, R.E., Samson, C. and Herd, R., 2006. Stony meteorite characterization by non-destructive measurement of magnetic properties. *Meteoritics and Planetary Science*, *41*, pp.355-373.

Stefan Mayer Instruments, 2017. Miniature Magnetic Field Sensor FLC 100. *Available online:* http://www.stefan-mayer.com/images/datasheets/Data-sheet_FLC-100.pdf

Suzuki, T., 2014. GNSS-Radar. *Available online:* http://www.taroz.net/GNSS-Radar.html

Takasu, T. and Yasuda, A., 2009, November. *Development of the low-cost RTK-GPS receiver with an open source program package RTKLIB.* In international symposium on GPS/GNSS (pp. 4-6). Jeju, Korea: International Convention Centre.

Welch, G. & Bishop, G., 1997. An Introduction to the Kalman filter. In Practice, 7(1), pp.1–16.

Welch, G. & Bishop., G., 2006. An Introduction to the Kalman Filter. *Department of Computer Science*, pp.27599-3175.

Wessel, P., and W. H. F. Smith, 1998. New, improved version of Generic Mapping Tools released, EOS Trans. Amer. Geophys. U., vol. 79 (47), pp. 579

Wijnberg. L, 2016. Good end results and comparison. Emlid Community Forum. *Available online:* https://community.emlid.com/t/good-end-results-and-comparison/1575

Wood, A., Cook, I., Doyle, B., Cunningham, M. and Samson, C., 2016. Experimental aeromagnetic survey using an unmanned air system. *The Leading Edge*, *35*(3), pp.270-273.

Zeets, S., 2016. REACH testing in the U.S. = Great Results! Emlid Community Forum. *Available online:* https://community.emlid.com/t/reach-testing-in-the-u-s-great-results/3017